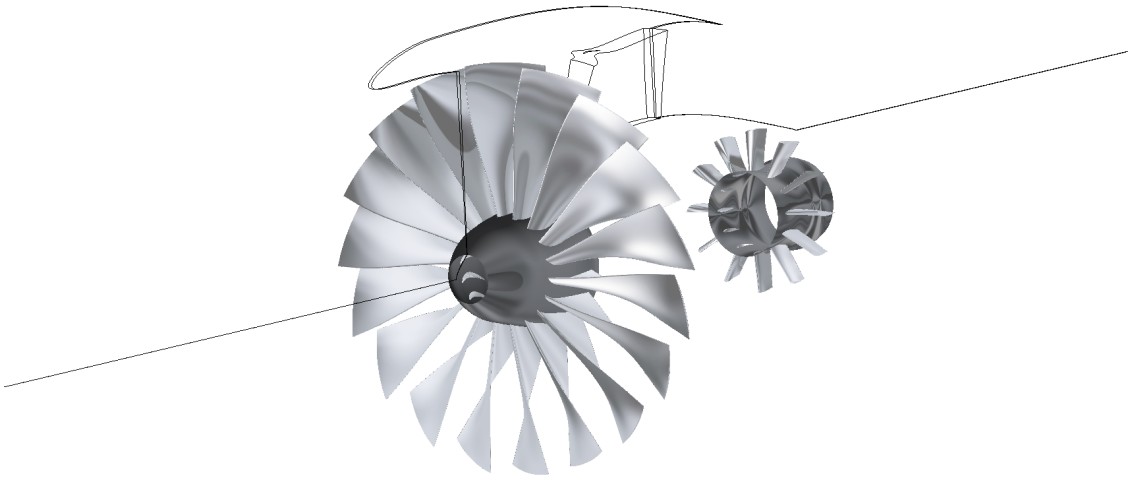

Aerodynamic design, optimization and acoustic analysis of a turbine rear structure

Master's thesis in Applied Mechanics

EMMA-LIISA WIKERBY

DEPARTMENT OF FLUID DYNAMICS

CHALMERS UNIVERSITY OF TECHNOLOGY
Gothenburg, Sweden 2024
www.chalmers.se

Master's thesis 2024

Aerodynamic design, optimization and acoustic analysis of a turbine rear structure

EMMA-LIISA WIKERBY

CHALMERS
UNIVERSITY OF TECHNOLOGY

Department of Applied Mechanics
Division of Fluid dynamics
Chalmers University of Technology
Gothenburg, Sweden 2024

Aerodynamic design, optimization and acoustic analysis of a turbine rear structure
EMMA-LIISA WIKERBY

Supervisor: Marcus Lejon, GKN Aerospace Sweden AB, Future Engines
Examiner: Tomas Grönstedt, Mechanics and Maritime Sciences

Master's Thesis 2024
Department of Applied Mechanics
Division of Fluid Dynamics
Chalmers University of Technology
SE-412 96 Gothenburg
Telephone +46 31 772 1000

Cover: Rendering of the fan and the TEC with a 2D contour of the RM400 engine.

Typeset in LaTeX
Printed by Chalmers Reproservice
Gothenburg, Sweden 2024

Aerodynamic design, optimization and acoustic analysis of a turbine rear structure
EMMA-LIISA WIKERBY
Department of Applied Mechanics
Chalmers University of Technology

Abstract

Noise emissions emanating from aircraft engines in urban areas has long been a concern. For this thesis the Turbine Rear Structure (TRS) of a turbofan engine is designed with the aim of reducing noise emission and total pressure losses. The aerodynamic functionality of the TRS is to de-swirl the upstream flow coming from the low pressure turbine to maximize the thrust for varying loading conditions. The objectives are thus to construct an aerodynamic design that work well at on- and off-design conditions and analyze the effect of leaned guide vanes on noise emissions. Through a Design of Experiment a design matrix is constructed with varied geometrical parameters for the guide vanes and endwalls by running the designs in a 3D solver. The design matrix gives the subspace for optimizing the TRS towards the objectives of this thesis by applying criterion on performance parameters. With an optimized design at the different loading conditions, lean is applied to the guide vanes and the effect of lean is then analyzed on the performance and noise emissions for the TRS.

Keywords: TRS, design of experiment, guide vanes, pressure loss, lean, aerodynamic performance, noise emissions

Acknowledgements

I would like to thank my supervisor Marcus Lejon for your great help and guidance throughout this project. I would also like to thank Mattias Billson for sharing your knowledge and guiding me through the acoustic study. Thank you also Jonas Larsson for your help during the design process and sharing your knowledge. I would also like to thank other colleagues that has helped me along the way.

I would like to thank my husband Daniel Wikerby for your everlasting support.

Last but not least, thank you to my family and friends for all your support.

Emma-Liisa Wikerby, Gothenburg, June 2024

List of Acronyms

Below is the list of acronyms that have been used throughout this thesis listed in alphabetical order:

BPF	Blade Passing Frequency
DOE	Design Of Experiment
EA	Evolutionary Algorithm
EOR	End Of Runway
ICD	Intermediate Compressor Duct
LHS	Latin Hypercube Sampling
LPT	Low Pressure Turbine
PWL	Power Level
RPM	Revolutions Per Minute
TRS	Turbine Rear Structure

Nomenclature

Below is the nomenclature of indices, sets, parameters, and variables that have been used throughout this thesis.

Parameters

α	Swirl angle
c_0	Blade surface velocity
C_{ax}	Axial chord length
C_D	Dissipation coefficient
C_{in}	Inlet velocity
C_p, C_{p0}	Static pressure coefficient and total pressure coefficient
C_{pb}	Pressure coefficient for wake loss
C_s	Vane surface length
Δp_0	Total pressure difference between inlet and outlet
ΔS	Entropy change
ϵ	Absolute value of the total pressure loss between flow conditions
H	Boundary layer
$l_{TE,throat}$	Trailing edge throat length
ν	Kinematic viscosity
$\dot{m}$	Mass flow rate
p_0	Total/stagnation pressure
p	Pressure
Re	Reynolds number
ρ	Density
s	Specific entropy
S	Total entropy
τ	Maximum thickness to axial chord ratio

t_{TE}	Trailing edge thickness
T	Static temperature
U_∞	Free stream velocity
ξ	Entropy loss coefficient
x_0	Effective length of turbulent boundary layer
x	Equivalent length of boundary layer
y_{span}	Coordinate in y direction, along the span of the vane

Subscripts

EB	Endwall Boundary
ref	reference
s	Vane suction side
p	Vane pressure side

Contents

List of Figures

List of Tables

1
Introduction

1.1 Background

With the development of aircraft engines comes a need for reducing noise emissions. This thesis is a part of the VIFT-project, funded by VINNOVAs NFFP8 programme, which aims to investigate reduction of noise emissions of a turbofan engine. The investigated engine is planned to enter service in year 2035 and is a development of the current engine RM400 [10]. Using computational methods the noise emissions can be evaluated for various design choices. In this project, various designs of a turbine exhaust vanes are designed and evaluated to estimate these emissions.

1.2 Purpose and Goals

The goal is to perform the aerodynamic design of a turbine rear structure that fit downstream of a low-pressure turbine designed by Lund university as part of the VIFT project. As part of the design process, an optimization tool will be used to find a design which perform well at a specified design point (top of climb) as well as an off-design condition (takeoff: end of runway). Furthermore, an analysis will be done to investigate the impact of the design parameter lean for the turbine exhaust vanes on the noise level from the engine core outlet. Tools that are used are GKN in-house design and meshing tools, ANSYS CFX and Python.

1.3 Recent work of turbine rear structures

Understanding of of aerodynamic behavior of turbine blades under various loading conditions is essential when estimating performance of a turbofan. For this reason a literature study is made for designs of turbine rear structures (TRS) and aerodynamic analysis. In following articles TRS guide vanes are studied for performance of swirl angle distribution and total pressure loss in outlet regions.

The TRS is a structural connector from the engine to the aircraft wings where the guide vanes are structural connectors to the casings of the TRS. In an engine realistic configuration, some guide vanes are thicker for allowing a passage of oil to the engine [19]. Aerodynamically, the TRS are designed to de-swirl the incoming flow from the LPT without producing high pressure losses, to provide an axial flow out from the engine for maximum thrust, see figure 1.1.

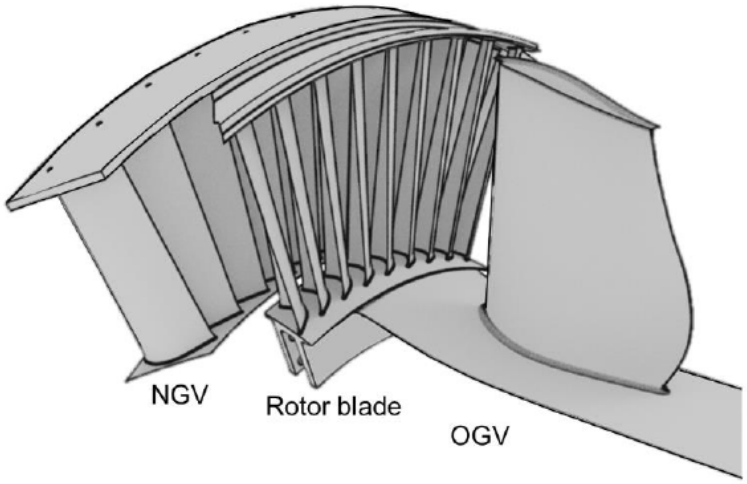

Figure 1.1: LPT and TRS vanes visualization of configuration from Vikhorev, V. et al [17].

When designing the TRS various geometrical parameters affect the flow through the passage such as endwall geometry, vane geometry, inlet flow from the LPT and different loading conditions [17].

1.3.1 Study of engine-realistic turbine rear structure

Vikhorev et al. [18] studied a TRS aerodynamically in an engine-realistic rig located at Chalmers University of Technology at three different flow conditions of on-design $\phi = 0.622$ and two off design conditions: low load $\phi = 0.588$ and high load: $\phi = 0.657$. The TRS has 12 outlet guide vanes (OGV) with a 30 degree spacing and has an inlet Reynolds number of 235000 for all loading conditions based on inlet channel height. The paper evaluates three different vanes designs of regular, thick and bump vanes. TRS are are needed for structural support as well as de-swirling the upstream unsteady high swirled flow from the LPT in order to maximize thrust. By having a gearbox between the fan and low-pressure shaft connecting the LPC and LPT, the loading of the fan becomes less so that the loading conditions in the LPT can operate at higher rotational speeds but none the less, the flow through the TRS should not produce separation in order to maximize performance and minimize loss. Therefore this study is crucial in understanding aerodynamic TRS performance.

The performance of the TRS was evaluated by measured total pressure and swirl angles upstream and downstream of the TRS in ref [18]. At the vane surface, static pressure was measured at the spans of 12.5 25, 50, 75 and 87.5 percent. Flow behaviors were captured using an oil-film visualization of the boundary layers. Streamlines were seen to migrate from the hub and shroud endwalls toward mid span which shows the increased thickening of boundary layer near the trailing edge. Local flow separations were seen at the vane suction side at on-design condition which appears due to secondary flows from the hub. At higher loading condition, reversed flow was

seen close to the hub side of the trailing edge.

Figure 1.2 shows the static pressure coefficient over the regular and thick vanes [18] where it can be seen that the thick vane results in higher blockage with increased acceleration and decreased static pressure at the peak suction point. This results in a more adverse pressure gradient (increased diffusion), making it more sensitive to separation. The decrease in static pressure is caused by the local curvature and passage area contraction, and between the two vane designs the maximum point of acceleration did not change noticeably. With increased loading, the minimum static pressure point moves upstream towards the leading edge of the vane profile. The increased loading conditions show regions of deceleration and local separation with reattachment for both regular and thick vanes, which is due to local laminar-turbulent transition with re-attachment of the boundary layer.

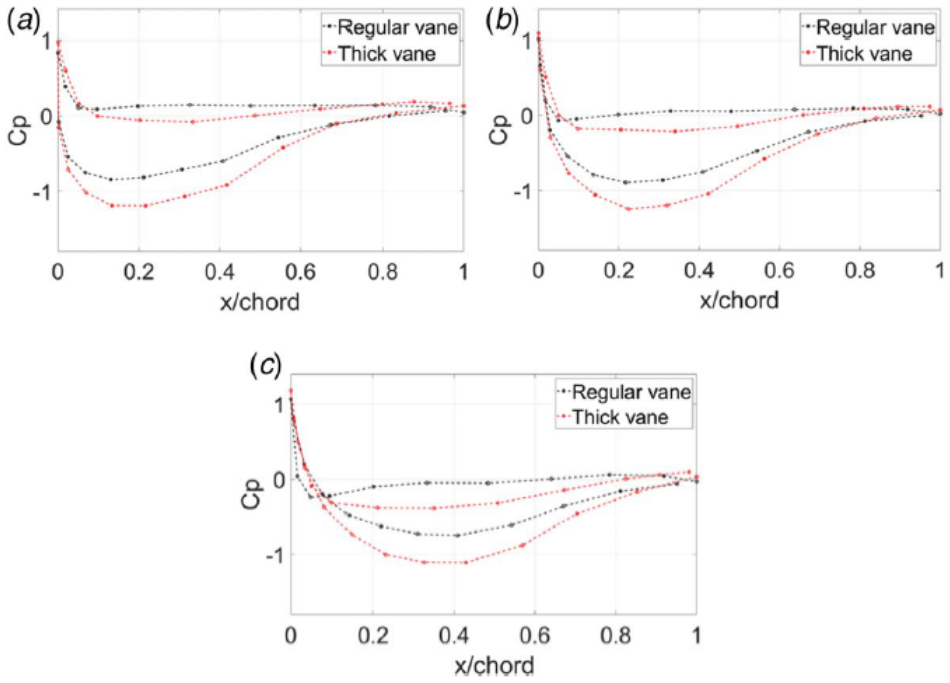

Figure 1.2: Static pressure coefficient distribution for regular and thick vane designs at design flow conditions shown at a) 25% span b) 50% span and b) 75% span from Vikhorev. V et al [18].

The total pressure was measured at inlet and outlet over a 30 degree sector. Looking at the total pressure drop at the inlet, a drop in pressure can be seen close to the hub [18]. This is caused by the secondary flows coming from the upstream LPT. Similar to the inlet, a total pressure drop is observed at the outlet close to the hub suction side. Comparison between CFD and experimental results show that total pressure contours of the wake show similar results between regular and thick vanes which indicate that loss generations do not show significant changes for increased thickness. Despite the similarity, a slight decrease in total pressure close to the hub

in the wake and thus indicating on an increase in loss.

Looking at the swirl angle distribution at the inlet [18], in figure 1.3a, the swirl angle decreases in magnitude and increases for the lower and higher loading conditions respectively. The swirl is seen to be the highest close to the hub and varies between -40 to -30 degrees between the loading conditions. Along the span, the swirl angle increases and reaches 10 to 20 degrees close to the shroud, depending on flow condition. The swirl angle distribution at the exit in figure 1.3b show that the flow is overturned for low loading condition and underturned for high loading condition both for a magnitude within 1 degree from the design-point. For the analyzed operating conditions, the exit swirl angle is within +-2 degrees from 10% to 90% span at the low loading condition, and within -+4 degrees at the high loading condition.

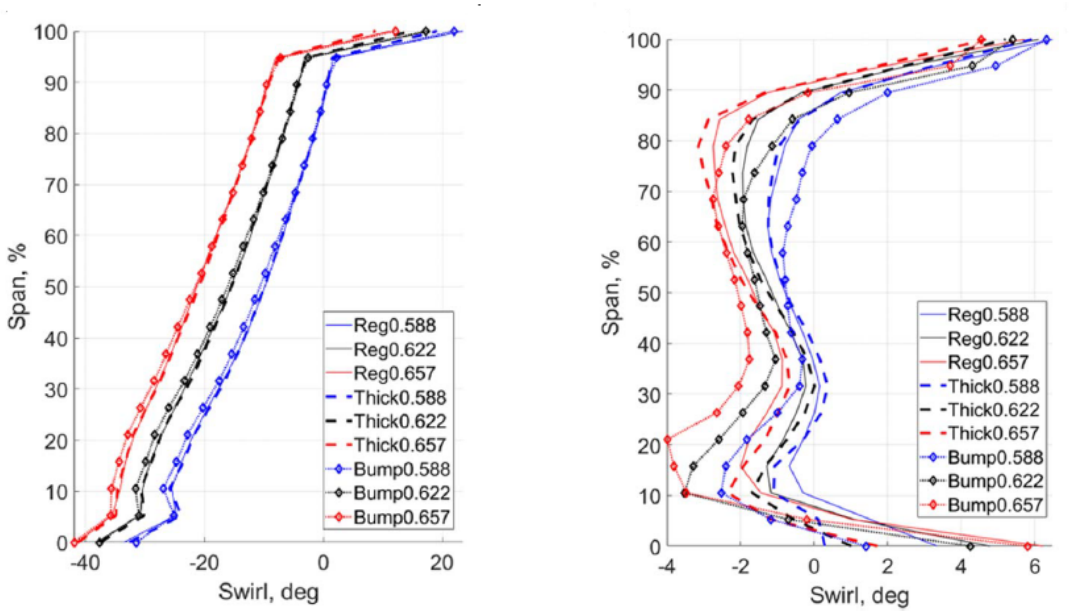

(a) Inlet boundary swirl angle distribution.

(b) Outlet boundary swirl angle distribution.

Figure 1.3: Circumferentially averaged swirl angle distribution along the span at inlet and outlet for the TRS in Vikhorev, V. et al [18].

In summary, the main difference between the regular and thick vanes show that for the latter the static pressure increases and shows that the vane design is more sensitive to separation. However the suction peak location seemed to remain the same for the same flow condition between both designs. When analyzing the increased loading, the suction peak moves upstream towards leading edge and local laminar-turbulent transition with re-attachment occurs. The increased maximum thickness of the vane design and increasing loading conditions should be taken in to account the increase in risk of separation. Besides the affects of the vane design on aerodynamic performance, the different flow conditions show the largest affect on the flow at the outlet of the TRS in terms of outlet swirl angle and total pressure.

1.3.2 Lean angle

A comparison between radially straight and leaned configuration of guide vanes in a TRS is studied by Vikhorev, V. et al [20]. An aerodynamic study of TRS OGVs typically show a radial pressure gradient, which causes streamlines to migrate towards mid-span when the flow crosses the vane surface from the leading edge to the trailing edge. In [20] the radial pressure gradient is larger at the suction side of the vane, close to the hub and for critical loading conditions this can result in a hub corner separation unless taken into account during the design process. By applying a positive lean of 20 degrees in the radial direction, giving an obtuse angle at the suction side seen in figure 1.4, the pressure gradient is shown to decrease. More specifically the aerodynamic and acoustic performance is shown to have a positive effect from leaned guide vanes.

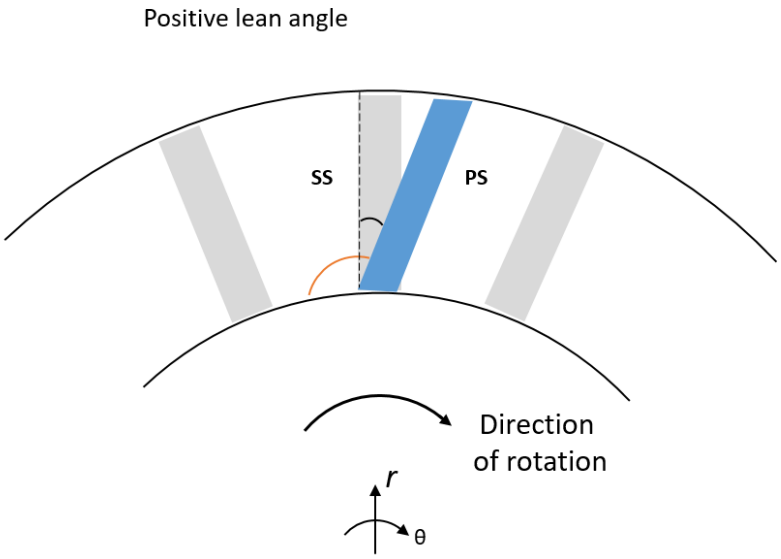

Figure 1.4: Illustration of positive lean angle of guide vanes. The image is shown in the cylindrical r-θ plane and shows the suction side (SS) and pressure side (PS) of the guide vane. The obtuse angle that occurs is marked in orange at the vane suction side, for a positive lean angle shown in black.

The effects of leaned guide vanes was studied for an engine-realistic turbine rear structure with a configuration of zero lean (radially stacked vanes) and leaned vanes with positive straight lean. Three different loading conditions were evaluated for an engine realistic Reynolds number based on a low-pressure exit swirl angle. Regular, thick and bump vanes were evaluated. A configuration of 18 guide vanes was designed in [20] were setup and was designed for shortened axial chord length and thickness to match the solidity of the TRS rig [18] where 12 straight radially stacked vanes. By leaning the guide vanes, the length in stacking direction of the vanes increase. Measurements for the TRS is taken at the inlet and outlet of a 30 degree sector with a azimuthal resolution of 0.6 degrees and radial resolution of 9.7 mm.

For the on-design loading condition for the regular and thick vanes the outlet total pressure showed a decrease in losses for the leaned guide vanes compared to the radially stacked vanes and is due to the change of the pressure gradient. Since thicker vanes become more diffusive at the suction side of the vane the vanes become more sensitive to separation, and in this case the leaned guide vanes show good aerodynamic performance in terms of low loss and no indication on separation. Total pressure coefficient contours at off-design conditions with low and high loading show that the leaned guide vanes have a decrease of the total pressure coefficient gradient at the suction side and losses are decreased. As for the on-design the thick leaned guide vanes show lower losses at both off-design conditions.

In summary, the leaned configuration of the guide vanes show that the radial pressure gradient is redistributed at the vane suction side and diffusion is reduced near the hub.

2

Theory

Geometrical parameters which are studied for the design task are explained in this section. This theory is applied and described in the next section.

2.1 Geometrical features of vanes

Camber angle is the angle between the blade inlet and outlet angles, seen in figure 2.1. The inlet and outlet camber angles, θ_{in} and θ_{out} are evaluated for the blade angles at leading and trailing edge respectively.

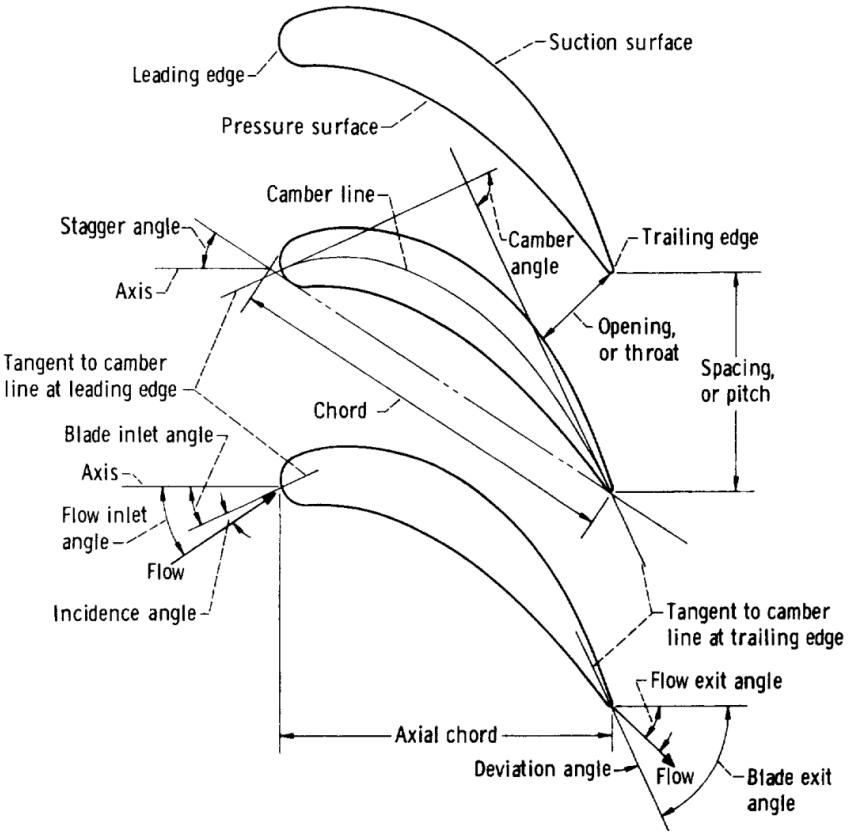

Figure 2.1: Vane nomenclature, angle definitions, figure from [7].

Maximum thickness location is the point along the chord where maximum thickness occurs, shown in figure 2.2.

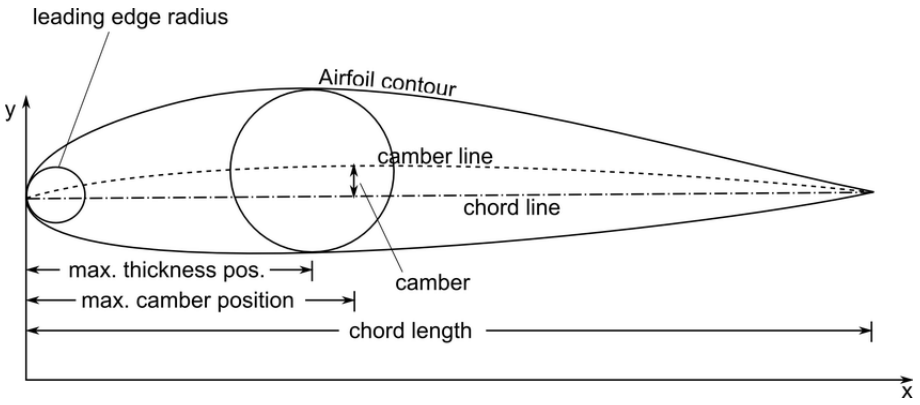

Figure 2.2: Vane airfoil geometry nomenclature, figure from [6].

2.1.1 Swirl angle

Swirl angle, in equation (2.1), is the angle between the circumferential velocity c_θ and meridional velocity c_m.

$$\alpha = tan^{-1}\left(\frac{c_\theta}{c_m}\right) \tag{2.1}$$

$$c_m = \sqrt{c_x^2 + c_r^2} \tag{2.2}$$

2.1.2 Lean and sweep of vanes

By adding lean to a vane is to circumferentially lean the blade along the stacking line, seen in figure 2.3. This can be done for a positive or negative lean with respect to the rotational direction. A sweep angle is applied to the vane in the flow direction along the stacking line, and can be done by a forward or backward sweep, which is also seen in the figure.

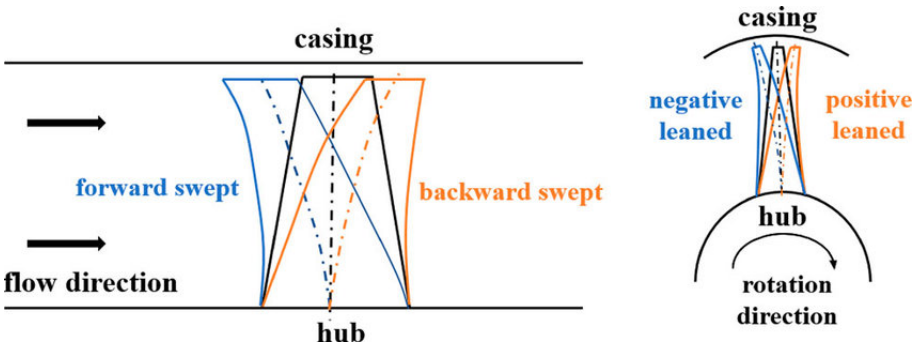

Figure 2.3: Definition of lean and sweep of vanes, figure from [22].

The solidity is calculated as the axial chord over pitch.

2.2 Pressure coefficient

Pressure variations through the turbine exhaust vanes are analyzed using the total and static pressure coefficients c_{p0} and c_{ps} in equations (2.3) and (2.4). The total pressure is defined as equation (2.5) and is calculated with the compressible flow relation [11], where the specific heat ratio γ is calculated for air.

$$c_{p0} = \frac{p_0 - p_{0,ref}}{p_{0,ref} - p_{s,ref}} \tag{2.3}$$

$$c_{ps} = \frac{p_s - p_{s,ref}}{p_{0,ref} - p_{s,ref}} \tag{2.4}$$

$$p_0 = p_s \left(1 + \frac{\gamma - 1}{2} M^2\right)^{\frac{\gamma}{\gamma - 1}} \tag{2.5}$$

2.2.1 Stratford shape

When analyzing the static pressure coefficient along the vane surface, Stratford [15] describes how a Stratford shape of the static pressure could show where diffusion occurs along the vane surface, see figure 2.4. The Stratford shape is seen in the static pressure coefficient plot at the suction side. The shape is seen from the maximum suction peak (near the maximum thickness location) where the static pressure is the lowest, towards trailing edge. The amount of turning of the flow determines how much diffusion that occur in the flow. By affecting the local diffusion, the loading of the vane can be placed close to the leading edge, making it front-loaded, or close to the trailing edge making it rear loaded. The amount of loading is calculated by the integral of static pressure over a span profile, where a higher integral of static pressure is a direct indicator of an increase in need of how much the flow needs to be turned.

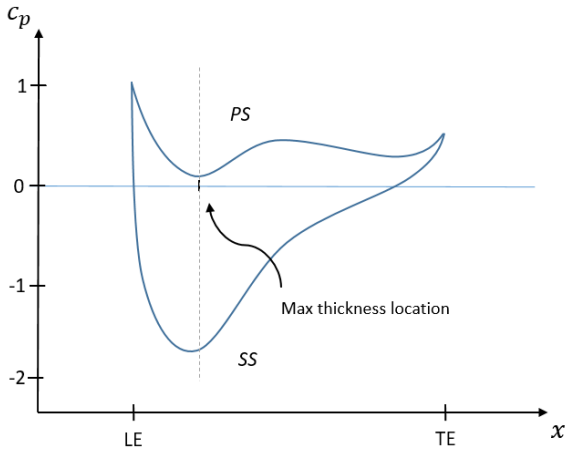

Figure 2.4: The image shows an example of the static pressure coefficient distribution over a vane surface at suction side (SS) and pressure side (PS).

2.3 Loss prediction

In turbomachinery it is prominent to find a design for which losses are minimal. This ensures a design aimed for higher overall efficiency of the system, but is not always easy to predict [3]. There are different losses to consider, see illustration in figure 2.5. Dentons loss prediction in turbines [4] considers boundary layer loss, tip leakage loss, trailing edge loss, endwall losses and shock loss, in terms of entropy changes. Inlet dynamic pressure is used for reference [12].

Loss mechanisms described in this section is considering axi-symmetrical flow in turbomachinery. Usual methodology for predicting losses in a blade row assume that flow features are not fully irreversible and thus the losses should be estimated with the entropy increase through the blade passage, rather than estimating in terms of only isentropic flow [5]. Therefore the loss estimations in this section is considering the entropy increase through the passage. For this project the flow is intended to adiabatic, leading to the assumption of neglecting heat transfer and only thermodynamic irreversibilities are contributing to the entropy increase.

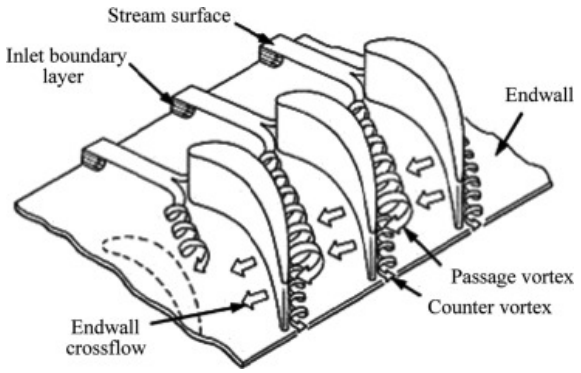

Figure 2.5: Illustration of losses in passage of turbomachine vanes, figure from [9].

2.3.1 Loss estimation

General loss estimation is evaluated by the fraction between the total pressure Δp_0 and total pressure at the inlet $p_{0,in}$, seen in equation (2.6).

$$\xi_{est} = \frac{\Delta p_0}{p_{0,in}} \tag{2.6}$$

2.3.2 Boundary layer loss

Boundary layer loss, also known as profile losses, are mainly considered in 2D profile vane analysis. Equation (2.7) shows the calculation for the boundary layer loss ξ_{BL} generated by entropy increase due to boundary layer formation in turbine nozzle vane passage [4]. The entropy generation is calculated for the sum of pressure from suction side "s" to pressure side "p". The dissipation coefficient C_D is estimated for the laminar case of $C_D = 0.002$, which is defined over the vane boundary layer. C_s is the vane surface length, x is the vane surface distance between suction and pressure

side, p is the pitch (circumferential distance between vanes), α_{ref} is the reference flow angle and the velocities c_0 and c_{ref} are the blade surface velocity and reference velocity.

$$\xi_{BL} = 2\sum_{s}^{p} \frac{C_s}{p \cdot cos(\alpha_{ref})} \int_0^1 C_D \rho \left(\frac{c_0}{c_{ref}}\right)^3 d(x/C_s) \tag{2.7}$$

2.3.3 Endwall loss

Endwall losses are caused by the annulus wall boundary layers, at the hub and shroud. The boundary layer loss is given as a 3D effect and can be estimated through the rise in entropy, according to Denton [4]. It is stated that the losses mainly depend on the entropy change. Equation (2.8) shows the endwall boundary layer loss for turbines ξ_{EB}, where the entropy ΔS_{EB} is calculated with equation (2.9) [12]. Seen in figure 2.5 the endwall losses generates vortices close to the endwalls and vanes.

$$\xi_{EB} = \frac{T}{\Delta S_{EB}} \frac{1}{\frac{\dot{m} c_{in}^2}{2}} \tag{2.8}$$

$$\Delta S_{EB} = 0.25 \int_0^{l_{ax}} \frac{C_D}{T} \left(\frac{c_s^4 - c_p^4}{c_s - c_p}\right) y_{span} dx \tag{2.9}$$

2.3.4 Wake loss

As the boundary layer forms on the vane and grows toward the trailing edge, wake losses are induced due to the streamline disruption downstream of the trailing edge [5]. The wake loss is calculated with the pressure coefficient of C_{pb}, trailing edge thickness t_{TE} and trailing edge throat length $l_{TE,throat}$, seen in equation (2.10).

$$\xi_{wake} = C_{pb} \frac{t_{TE}}{l_{TE,throat}} \tag{2.10}$$

2.4 Stratford's separation criterion

The Stratford separation criteria is a prediction of separation of turbulent boundary layers. The criterion is evaluated with equation (2.11) where the pressure coefficient C_p is solved for and is calculated from the point of minimum static pressure and main stream velocity U_∞ [15]. Depending on the second derivative of the pressure, the coefficient k is chosen according to table 2.1. The equation estimates boundary layer separation for when the skin friction is zero.

$$C_p \left(x \cdot \frac{dC_p}{dx}\right)^{\frac{1}{2}} = k \cdot (10^{-6} Re)^{\frac{1}{10}} \tag{2.11}$$

Table 2.1: Coefficient k in Stratford's separation criterion depending on the second derivative of the pressure.

	$C_p = \frac{4}{7}$
$\frac{d^2p}{dx^2} \geq 0$	k=0.39
$\frac{d^2p}{dx^2} < 0$	k=0.35

If the boundary layer transitions is assumed to undergo direct turbulent boundary layer formation the equivalent length x is estimated by calculating the effective length of the boundary layer x_0, see equation (2.12), where upstream at the leading edge the pressure is constant and main stream velocity U_∞ is maintained. X is the distance to the leading edge and X_0 is the distance between a fictitious stagnation point for a flat plate of constant pressure to the boundary layer. The equation is thus only valid for Reynolds number above 10^6.

$$x_0 = \int_0^{X_0} \left(\frac{U}{U_\infty}\right)^3 dX \tag{2.12}$$

By assuming fully turbulent boundary layer the Reynolds number is calculated by equation (2.13).

$$Re = \frac{U_0 x_0}{\nu} \tag{2.13}$$

When the pressure gradient is higher than the criterion $C_p > \frac{4}{7}$ the pressure gradient is calculated to match the derivative of $C_p = \frac{4}{7}$ by calculating equation (2.14) where x_0 and $\frac{dC_p}{dx_0}$ is calculated for $C_p = 4/7$ in the equations for a and b (2.15) and (2.16) [16].

$$C_p = 1 - \frac{a}{(x_0 + b)^{\frac{1}{2}}} \tag{2.14}$$

$$a = \frac{3}{7}(x_0 + b) \tag{2.15}$$

$$b = \frac{3}{14\frac{dC_p}{dx_0}} - x_0 \tag{2.16}$$

The criterion is then evaluated by re-arranging equation (2.11), shown in equation (2.17). When the criterion is negative the flow separates, while a positive value indicates that separation is not occurring.

$$\text{Stratford criterion} = k \cdot (10^{-6} Re)^{\frac{1}{10}} - C_p \left(x \cdot \frac{dC_p}{dx}\right)^{\frac{1}{2}} \tag{2.17}$$

2.5 Latin-Hypercube Sampling

When generating a number of designs in a DOE, Latin Hypercube Sampling (LHS) is used in order to statistically generate a design space for multi-dimensional distribution of parameter values [13]. The LHS divides the parameter intervals into

equal sampling points of N designs and K parameters. A sampling matrix of NxK is created with LHS where a division of the N space is divided into equal distributions and where each of the samplings N are randomly distributed within this sampling space for each variable K.

LHS is generally described by the latin square design (two dimensional) with rows and columns where each row and column contain an individual parameter value, see table 2.2. Extending this to a multidimensional parameter space gives the defined Latin Hypercube.

Table 2.2: Latin square plane of two dimensional parameter space.

	K1		
K2	x		
			x
		x	

Each parameter is specified for a range where the LHS randomly distributes the parameter in the equally subdivided space for a random value within each subspace. Given this distribution, each parameter is given an individual parameter value.

2.6 Evolutionary algorithm

When optimizing a design, various methods for finding the optimal design can be used. In this thesis the evolutionary algorithm (EA) [2] is used. The evolutionary algorithm takes a data set (in this case, a data set of designs) as a first population. By assigning fitness values to each design, the algorithm then selects which data points in the data set that undergoes reproduction (creates new designs) and categorizes them into archive and offspring individuals. Evaluation of the new population and assigning new fitness values creates the new group of individuals for which a new generation is created through the same process. The algorithm repeats this process of creating generations until the the numbers of generations is met or if the algorithm stagnates and the best individuals (designs) has been generated. Since this thesis aims to optimize for a range of design variables, the evolutionary algorithm is suited due to the application of multi-variable designs.

How the algorithm creates the new designs can be made i various ways. For this thesis the new designs are created only from the data set which makes the optimization try to resemble new design sets from known data. By assigning objective functions, criteria, limits or constraints on the parameter range and responses, a response surface creates the subspace for which the evolutionary algorithm reads the first population of data.

2.6.1 Pareto front

Through the optimizer, a Pareto 2D plot is created where all designs are plotted against given objective functions for which the designs are optimized towards. The

Pareto 2D plot shows which designs that can handle given objectives, constraints or limits [2]. A front is also plotted for the non-dominated designs for which there are no better designs that meet the objective functions. In figure 2.6 a Pareto 2D plot is shown for two objective functions, where the non-dominated designs are shown in the black filled scatter plot.

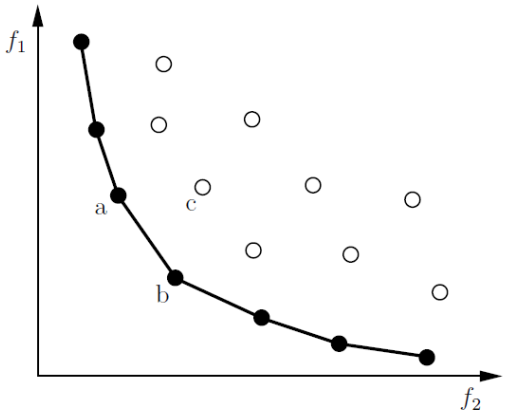

Figure 2.6: Pareto 2D plot shown for two objective functions $f1$ and $f2$ where example designs a, b and c are marked. The black filled line plot shows the Pareto front 2.6.

2.7 Wall functions

For a turbulence model using wall functions the layers close to the walls will be within viscous sub-layer, log-law layer of in the outer layer. For the k-ω models a coarse mesh will automatically use wall functions for the wall layers and for a refined boundary layer mesh the Low-Re model will be applied [1] and is determined from the y^+ value, equation (2.18). y^+ is a dimensionless value where Δy is the distance between the wall and the first node of the first cell and u_τ is the friction velocity. Using a coarse mesh, with unrefined boundary layers, the y^+ range is valid within 30 to 300 (for k-ω turbulence models). Usually a resolved boundary layer is within at least 10 mesh nodes.

$$y^+ = \frac{\Delta y u_\tau}{\nu} \tag{2.18}$$

3
Optimization procedure

The current section describes the methods for generating designs and the procedure of creating the DOE design space which is used in the optimization. The designs for the ICD and TRS were run with boundary conditions at both design and off-design point, and the optimized design for the TRS were used in the acoustic study.

3.1 Vane and endwall design of ICD and TRS

The ICD aft of the two-stage low-speed low-pressure ratio axial compressor at Chalmers university [8] is re-designed. The compressor is derived from the two rear stages of the high-speed low-pressure compressor in the cluster engine RM400. The ICD is re-designed to find a less aggressive design which can be used as a starting point for future numerical studies of the compressor with and without bleed flow extraction. The task to re-design the ICD also provide an opportunity to learn the tools needed to subsequently design a TEC for RM400. The TEC that is being re-designed in this thesis is designed for minimized total pressure losses and lower noise emissions.

The designs of the ICD and TRS starts by creating a baseline design using boundary conditions at design-point and is analyzed from results run with a 2D solver and a 3D CUDA solver, which is a GPU-solver. Parameters for the endwall geometry contours and vanes geometry angles and lengths were determined through the 2D solver during the design process. The Maximum thickness to chord ratio τ was calculated as maximum thickness over axial chord. The maximum thickness was decided for a calculated axial chord length from the solidity. The solidity was determined for a design that can keep the boundary layers from separating while also being able to turn the flow. The axial chord length calculated from the solidity was also constrained to be keep within the given inlet and outlet axial coordinate specifications. When analyzing the vane design, the airfoil sections at 12.5%, 50% and 87.5% spans was evaluated as hub, mid and shroud sections. The reason for why 0% and 100% spans was not evaluated is that 3D flow features for the endwalls are not resolved using 2D solvers. A design for which the 2D aerodynamic performance at the different spans show a static pressure suction peak location close to the maximum thickness location and an outlet swirl angle profile as close to zero as possible was analyzed. The design was then run through the 3D solver for which the wall shear stress along the vane surface and total pressure was analyzed. Wall shear stress equal to zero would indicate that the flow is separated, therefore a non-zero positive value was

desired. The meshing in the inhouse tool Volvane, G3Dmesh is used for both ICD and TRS with 26 spanwise nodes, 35 streamwise nodes and 18 pitch nodes.

The endwalls are constructed by adding perturbations to the mean line and height distributions in equation (3.1), where r_s and r_h are the radii along the axial coordinate at shroud and hub respectively.

$$\begin{aligned} \tilde{m}(x) &= \frac{1}{2}r_s(x) + \frac{1}{2}r_h(x) \\ \tilde{h}(x) &= r_s(x) - r_h(x) \end{aligned} \tag{3.1}$$

Adjustments of the mean line and height distributions are made with orthogonal polynomials to a reference duct, by using two orthogonal non-zero polynomial basis functions P1 and P2 which satisfy the radial and axial inlet and outlet coordinates and curvatures [21], see equation (3.2), by keeping the same radial and axial corner points. The orthogonality of the polynomial is fulfilled according to equation (3.3) and the two basis functions that are used is shown in equation (3.4).

$$P_i(x) = \frac{dP_i}{dx} = \frac{d^2P_i}{dx^2} = 0 \text{ as } \begin{cases} x = 0 \\ x = L \end{cases} \tag{3.2}$$

$$\int_0^L P_i(x)P_j(x)dx = \begin{cases} = 0 & \text{as } i \neq j \\ \neq 0 & \text{as } i = j \end{cases} \tag{3.3}$$

$$\begin{aligned} P_1(x) &= x^3(L-x)^3 \\ P_2(x) &= x^3(L-x)^3(\frac{L}{2} - x) \end{aligned} \tag{3.4}$$

The mean line and height adjustments are shown in equation (3.5) with the two polynomials P_1 and P_2. The coefficients c and d are given certain values which is then multiplied with the basis functions and adds the modification to the reference geometry. The new endwall geometry of the hub and the shroud is then obtained by equation (3.6).

$$\begin{aligned} \tilde{m}^*(x) &= \tilde{m}^{ref}(x) + c_1P_1(x) + c_2P_2(x) \\ \tilde{h}^*(x) &= \tilde{h}^{ref}(x) + d_1P_1(x) + d_2P_2(x) \end{aligned} \tag{3.5}$$

$$\begin{aligned} r_h^*(x) &= \tilde{m}^*(x) - \frac{1}{2}\tilde{h}^*(x) \\ r_s^*(x) &= \tilde{m}^*(x) + \frac{1}{2}\tilde{h}^*(x) \end{aligned} \tag{3.6}$$

Following the design process and evaluation, a baseline design was created and used in the optimization process where parameters for the polynomials were adjusted within given minimum and maximum perturbation values $P1$ [mm] and $P2$ [mm].

3.2 Design of Experiments

Having the baseline design where the CUDA solver has calculated a design of minimized risk for separation (by calculating wall shear stress), the DOE is set up by

defining parameters and ranges of magnitudes. For example if the endwall design parameter 1 at the hub will be varied by 5 mm, the ranges will be within negative to positive magnitude of (-5, +5) mm.

The numbers of parameters K to vary in the DOE decides how many candidate designs N needed for constructing a second order polynomial from the response, given by the equation (3.7), which is used for the optimization in OptiSLang. This is the koshal quadratic sampling N of K numbers of variables [14].

$$N = \frac{(K+2)(K+1)}{2} \tag{3.7}$$

A DOE matrix is then generated with N designs with normalized values for the chosen parameters range (-1, +1) and real values which is varied in the design. This is generated by LHS which gives independent values for each row and column in a matrix for all parameter values. In the matrix the parameter ranges are generated for the actual range from the normalized design matrix when the DOE is run.

With all designs, a script with inputs of geometry, mesh and CFX settings containing boundary conditions (at on and off design) are run for each geometry. For the ICD a wall functions mesh is used and for the TRS a wall refined low-Re mesh is used. A criterion of 700 and 400 iterations are set for the ICD and TRS respectively, which was determined by monitoring output parameters of massflow and making sure it had stabilized in the CFX solver when running one of the designs with the same settings as for the DOE runs.

3.3 Optimization in OptiSLang

With the DOE runs at design and off-design points, the average swirl angle at outlet, separation surface area, total pressure loss at design point and the difference in total pressure loss between flow conditions, defined as $\epsilon = \mid p_{0,loss(Off-DP)} - p_{0,loss(DP)} \mid$, the TRS is evaluated.

Optimizing for a low loss design in OptiSLang [2] is made by using the DOE matrix and creating a MOP (optimized prognosis methodology). The designs from the MOP are then run through a post-processor in OptiSLang where a response surface in the form of a second order polynomial is created. The Response surface shows the most affecting variables on the given responses for each design from the MOP. With the results from the MOP, an optimization with an evolutionary algorithm is run in order to get an optimized design.

In the evolutionary algorithm constraints are set for maximum average outlet swirl angle and maximum separation surface area. The objective functions are set as:

1. minimize total pressure loss at the design point
2. minimize difference in total pressure loss ϵ

The second objective function is used to find a robust design. A great design would constitute a design with low total pressure loss at the design point, and a low increase in loss from the design to off-design condition.

The aim is to reduce the total pressure loss at design point as well as minimizing the absolute value between the total pressure losses, ϵ, at design and off-design point. For the ICD there are flow conditions of design-point and off design-point, ϵ is calculated for each design between the two flow conditions. For the TRS there are a design point and two off design points, whereby robustness is assessed by calculating the largest absolute difference between the two off-design points and the design point.

The results from the EA shows a Pareto 2D plot for each objective function prescribed to the EA. In this plot, from the Pareto front, the two Pareto designs at the end-points of the Pareto front, as well as one intermediate Pareto design, are chosen for further analysis using the CUDA solver and ANSYS CFX.

3.4 Acoustic analysis of TEC

One of the noise sources from the engine core exit (after the LPT and TEC) is the interaction between the wakes of the last LPT rotor stage and the TEC inlet. The source of the noise considered in this work is the tonal noise resulting from the LPT wake-TEC interaction. The tonal component originates from the frequency passing of the 108 rotor wakes by the 12 TEC struts which is a deterministic phenomenon which results in tones. The lowest frequency of the interaction defined by $\Omega \cdot N_{rotor}$ [rad/s] is called the 1st Blade passing frequency (BPF). Higher harmonics of the interaction are called 2nd BPF, 3rd BPF, etc, where the 2nd BPF is calculated as double the 1st BPS as $2 \cdot \Omega \cdot N_{rotor}$ and the 3rd BPF is three times the frequency and so on. Given the rotor RPM the 1st BPF is within human hearing levels (12500 Hz), while the 2nd BPF (25000 Hz) is too high to be heard. For this reason only the 1st BPF will be analyzed for the noise emissions.

3.4.1 Mesh

The high speed of the LPT and the large number of rotor blades in the last stage of the LPT relative to the number of TEC struts result in a significant mesh size since of the TEC the LPT wakes need to be sufficiently resolved to reduce the numerical dissipation in the solver. The interaction results in acoustic waves which will propagate within the TEC domain which also needs to be resolved. The mesh requirement based on the 1st BPF are 0.5 mm cell size in the tangential direction at the hub and 1 mm cell size at the shroud for 30 cells per wave length, and 2 mm cell size in the axial direction for 13 cells per wave length. Total mesh elements consisted of 11.3 million cells.

3.4.2 Solver

The simulations of the LPT-TEC interactions are done using the in-house solver Linnea, with boundary conditions at EOR. Linnea is a CFD code which solves the linearized Navier-Stokes equations in frequency domain. Linnea is based on the G3D family of codes. The equations are solved using a finite volume method with

second-order three-stage Runge-Kutta technique for time marching, low-dissipation third-order upwind-biased scheme for the convective fluxes and second-order centered difference approach for the diffusive fluxes. The Linnea code has highly absorbing boundary conditions to reduce the amount of acoustic reflections at the flow boundaries (Inlets and Outlets).

3.4.3 Analysis

The noise levels are evaluated for the power level which is calculated in the logarithmic scale according to equation (3.8) where P is the acoustic power (evaluated for the integrated energy over a surface) and P_{ref} is the reference power of 10^{-12}.

$$PWL = 10 \cdot \log\left(\frac{P}{P_{ref}}\right) [\text{dB}] \tag{3.8}$$

The waves moving through the TEC was analyzed from the entropy and pressure contours.

4
ICD design

Methods for designing the baseline design, optimizing and analyzing the design is described in this section.

4.1 Method

Designing the ICD, the endwalls and vane design is first constructed from given constraints of inlet and outlet radial and axial coordinates. Endwall corner points are set out by the coordinates show in table 4.1.

Table 4.1: ICD endwall radial and axial corner points.

	Hub	**Shroud**
Radial inlet coordinate [mm]	480.0	560.0
Radial outlet coordinate [mm]	230.0	360.0
Axial inlet coordinate [mm]	358.5	358.0
Axial outlet coordinate [mm]	770.0	770.0

The numbers of struts in the ICD are given to be 8. The vane LE axial coordinate for the hub is to be at least 60 mm from the hub inlet axial coordinate. This gave a leading edge axial coordinate location at the hub of 418.5 mm.

The vane geometry design parameters at hub, mid and shroud spans (12.5%, 50% and 87.5%) are designed to match the inlet flow angles and outlet flow angles which is desired to be close to zero. The vanes are stacked in a straight line at the maximum thickness location. A sweep angle of 20 degrees is set for the leading edge from hub to shroud.

4.1.1 Boundary conditions

Two flow conditions are used in the design process of the ICD and consists of the design point and off-design point which is the flow condition where the compressor is close to stall. Inlet boundary condition profiles are shown for both design and off-design points of swirl angle in figure 4.1, total pressure in figure 4.2 and total temperature in figure 4.3.

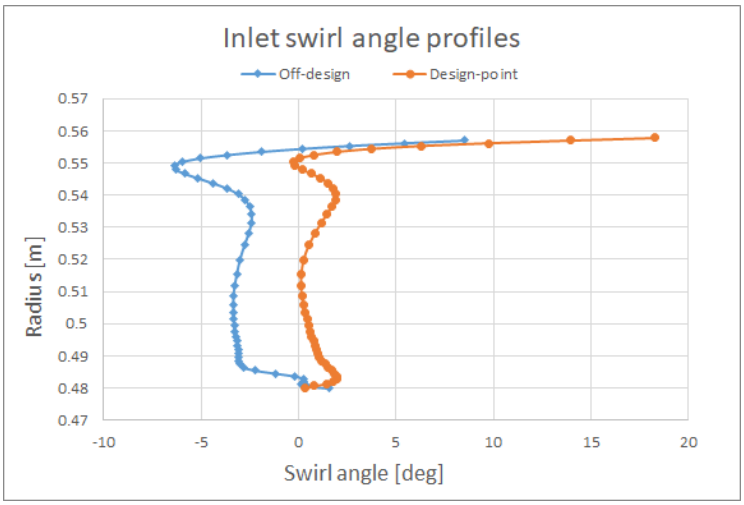

Figure 4.1: Inlet swirl angle profile for the ICD at design and off-design.

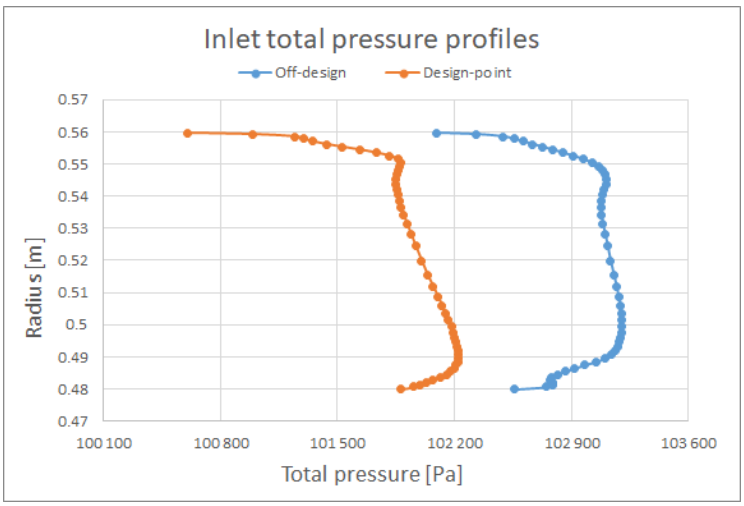

Figure 4.2: Inlet total pressure profile for the ICD at design and off-design.

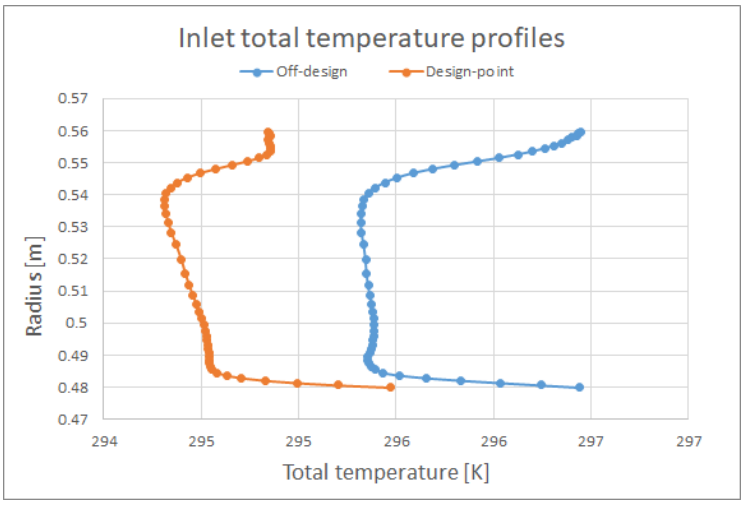

Figure 4.3: Inlet total temperature profile for the ICD at design and off-design.

4.2 Establishing a baseline design

In order to design the baseline design for the DOE and optimization, the endwalls and vane geometry design methods are shown and discussed. From the corner points of the ICD the endwall geometry is constructed with the maximum perturbations shown in table 4.2, by setting the endwall parameters such that the baseline design does not produce separation. Endwall plot for the ICD is shown in figure 4.4. The axial chord length is calculated from the solidity and the maximum thickness is calculated from the maximum thickness over axial chord length τ.

Table 4.2: Parameter values for the endwall baseline geometry.

	Hub	**Shroud**
P1 [mm]	-22	20
P2 [mm]	-15	5

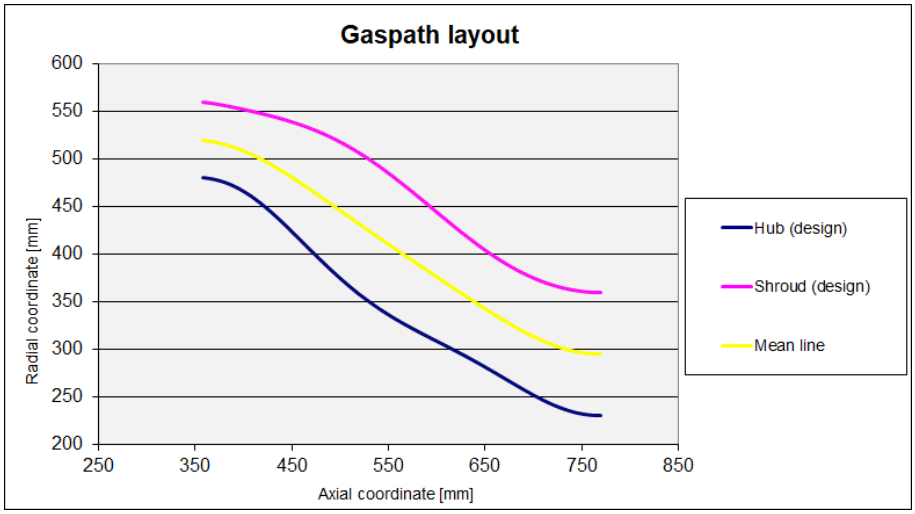

Figure 4.4: Gaspath endwall plot for the ICD.

The vane design is given equal parameter range, shown in table 4.3, for all spans and are stacked at maximum thickness, seen in figure 4.5. Note the difference of the scales in each direction.

Table 4.3: Baseline design of the ICD vanes at all spans

Span position of section %	All spans
Solidity	0.558
ϵ	0.167
Axial Chord [mm]	210
Max thickness [mm]	32.0
Max thickness location [%]	35.0
LE thickness [mm]	6.00
TE thickness [mm]	4.00

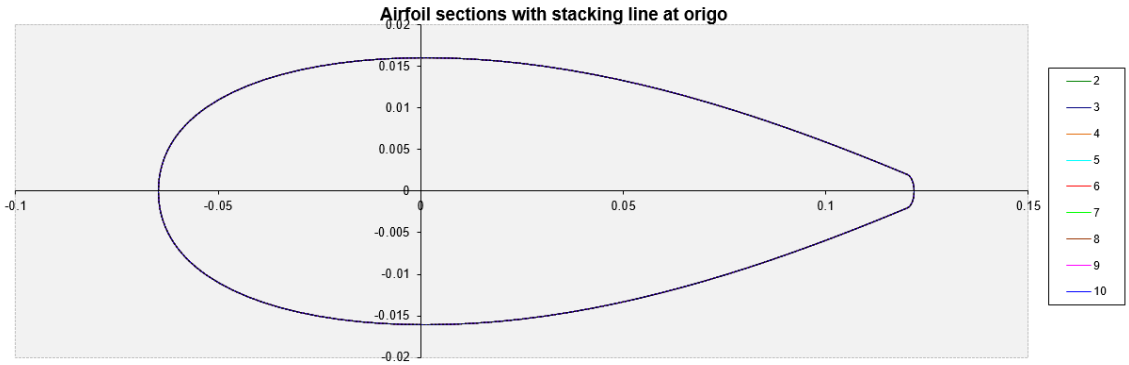

Figure 4.5: Vane geometry for the ICD of all spans. Plot view is in the stacking line at orgin of the plot.

The vane design is constructed by straight vanes, with zero camber angles, and a sweep angle of 20 degrees, seen in figure 4.6.

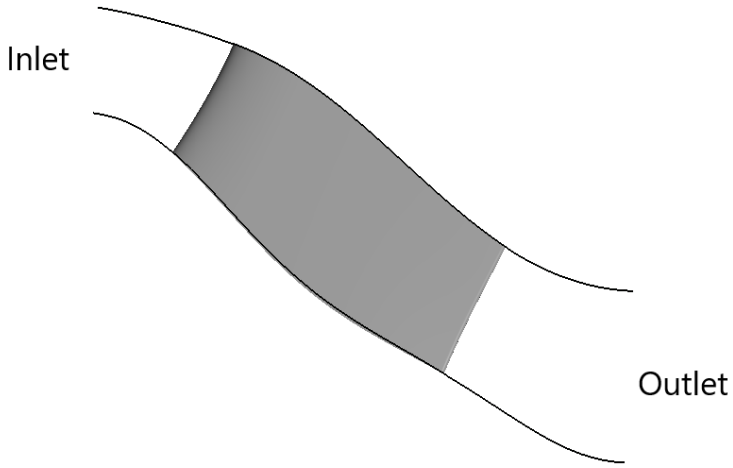

Figure 4.6: ICD baseline design showing a side view of the vane and endwall profiles. To the left is the inlet and to the right is the outlet.

An isometric view of the design is shown in figure 4.7.

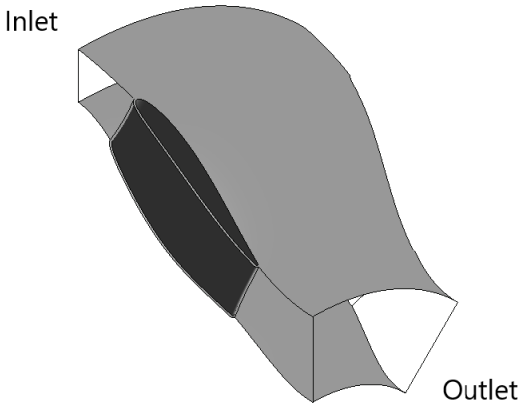

Figure 4.7: ICD baseline design showing an isometric view of the duct.

Analyzing the flow in volvane for the wall shear stress at the suction and pressure sides in figures 4.8 and 4.9.

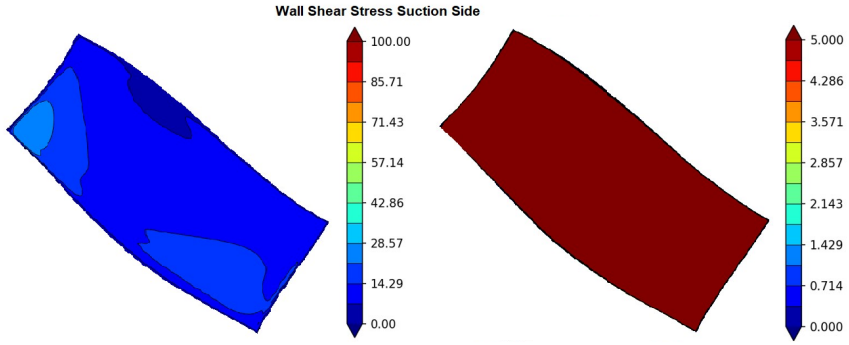

Figure 4.8: Wall shear stress contour plots of the ICD vane suction side, from the CUDA solver. Left figure shows the wall shear contour plot in the range of 0-100 Pa and the right figure shows the range of 0-5 Pa.

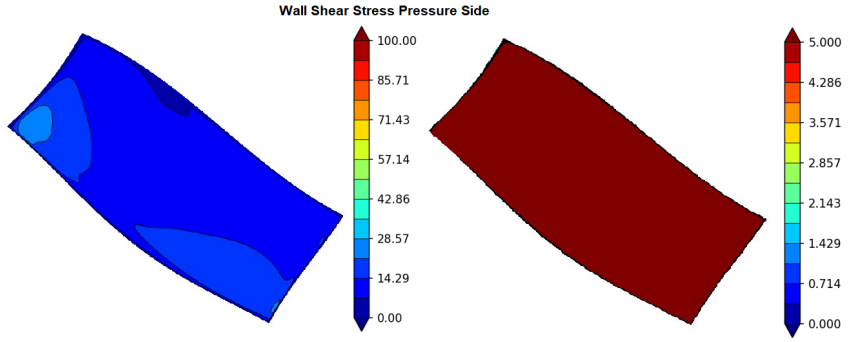

Figure 4.9: Wall shear stress contour plots of the ICD vane pressure side, from the CUDA solver. Left figure shows the wall shear contour plot in the range of 0-100 Pa and the right figure shows the range of 0-5 Pa.

4.2.1 Mesh

The mesh that was used in the DOE, when run in CFX, consists of 631120 mesh elements. The mesh is shown for isometric figure and top view in figures 4.10 and 4.11. For visualization purposes the two periodic sides, inlet and outlet are not shown in the mesh figures.

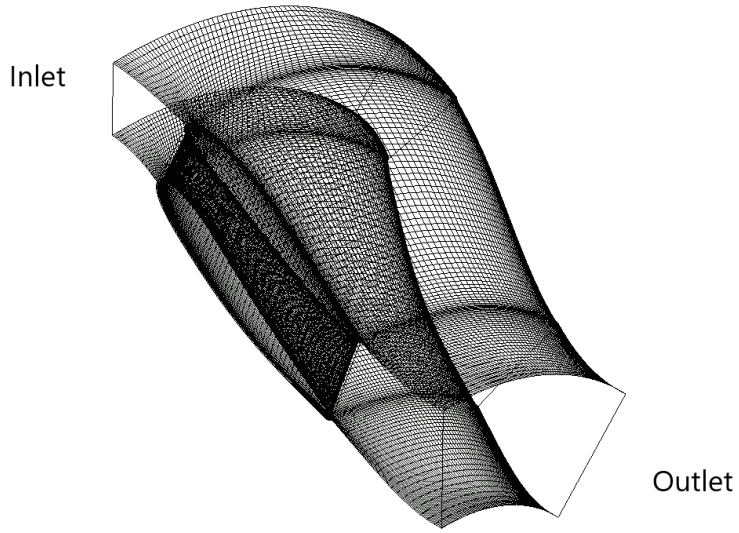

Figure 4.10: Isometric figure of the ICD mesh.

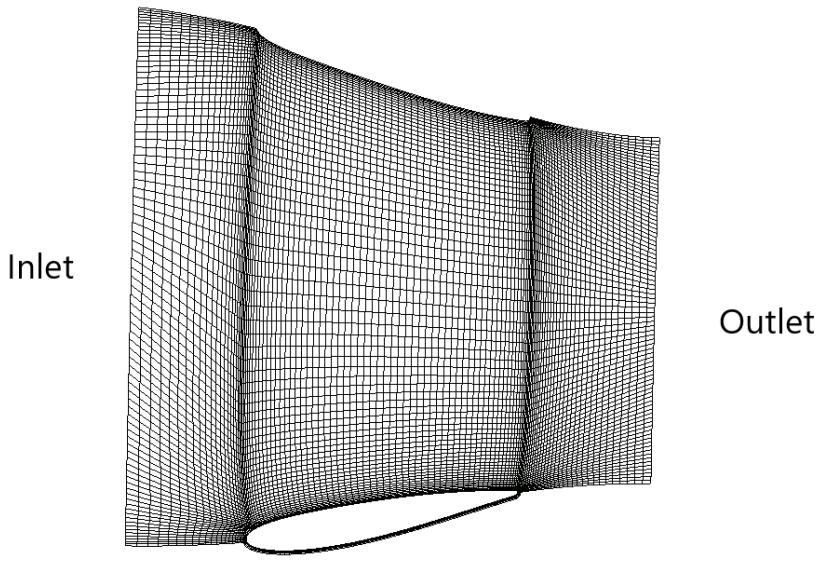

Figure 4.11: Top view of the shroud mesh of the ICD.

Shown in figure 4.12 the boundary layer is not refined as it was used with the k-ω turbulence model where wall function models will be used.

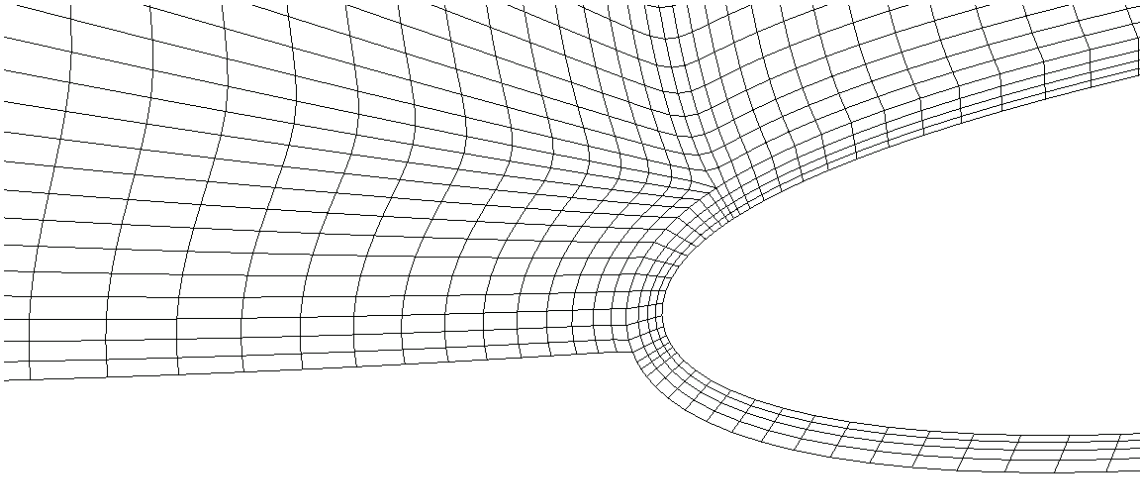

Figure 4.12: Zoom in on leading edge at the shroud of the ICD.

4.3 ICD design optimized in OptiSLang

Given the baseline design for the ICD, the geometries for the DOE were generated with the parameter range shown in table 4.4. From the koshal quadratic sampling equation (3.7) the numbers of designs that calculated was 45 designs, for 8 parameters that were varied for the geometry. In order to increase the accuracy of generating a response surface that predict the performance of the ICD in the optimization process, a decision of doubling the numbers of designs to 90 designs was made.

Table 4.4: Interval for values for parameters from DOE for endwall splines of maximum perturbation, axial chord, thickness and maximum thickness location. Total of 8 parameters were varied for the geometry and 90 designs were generated within the range values.

	Hub (12.5%)	**Mid (50%)**	**Shroud (87.5%)**
P1 [mm]	+/- 10	-	+/- 10
P2 [mm]	+/- 5	-	+/- 5
t_{loc}/C_{ax} [%]	+/- 10	+/- 10	+/- 10
Sweep [deg]	+/- 10	-	-

The DOE matrix is then imported into OptiSLang where parameters, response values and parameter IDs were defined and imported into the MOP, creating the response surface for the design space, seen in figure 4.13. From the MOP the response surfaces for the objectives of minimizing total pressure loss at design point and total pressure difference ϵ is shown in figures 4.13a and 4.13b. The design parameters in the response surface are the ones that have the greatest effect on the objective

functions and constraints. This entails that the P1 parameter for the endwalls at hub and shroud affects the objective functions of minimizing total pressure loss at design point. For the objective function of minimizing the total pressure difference ϵ the largest affects on the output is given by the parameters P1 at hub and sweep angle. The parameter output range for both objective functions are very small and a reason is that the criteria for the values for the constraints for the response values had been set to low, giving a narrow range of designs to optimize for.

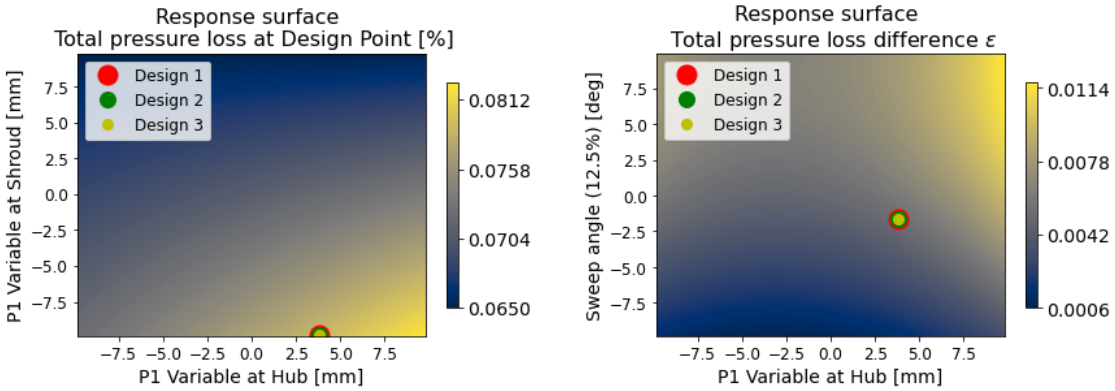

(a) Leading edge camber angle and P1 modification at shroud endwall.

(b) Leading edge camber angle and max thickness location.

Figure 4.13: Response surface contour plots for the ICD designs when running the DOE in the MOP in OptiSLang. Seen in the figures are also the designs which is chosen from the evolutionary algorithm optimization, described later in this section.

Given the response surfaces, the criterion for the evolutionary algorithm in order to optimize the design is set for the parameters and response in table 4.5. Deciding the values for the constraints was made by analyzing the results of average outlet swirl angle and separation surface area at both design and off-design point, by finding what the lowest values the designs could achieve. A value is then chosen close to those values, and run in the evolutionary algorithm. If the designs could not be optimized due to the constraints being too small (thus not being able to optimize towards the constraints and objective functions), the constraint values are increased until the optimization could generate a set of designs that fulfill the criteria.

Table 4.5: Criterion for the evolutionary algorithm of the ICD DOE in OptiSLang.

Criteria for evolutionary algorithm	
Average outlet swirl at DP [deg]	<= 0.01
Average outlet swirl at NS [deg]	<= 1
Separation surface area at DP $[m^2]$	<= 0.003
Separation surface area at NS $[m^2]$	<= 0.003
P0 loss at DP	MIN
P0 loss difference ϵ	MIN

The evolutionary algorithm ran 1000 designs, creating a Pareto 2D plot in figure

4.14 for the designs that passed the constraints (the black scatter plot) and the ones that violated the constraints (grey scatter plot). From the Pareto front (red scatter plot) three designs of are chosen to be analyzed as to decide on an optimal design for the ICD.

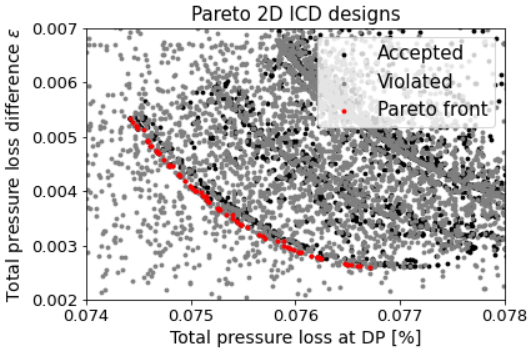

(a) Zoom in on the pareto front for fulfilled, violated, and pareto designs.

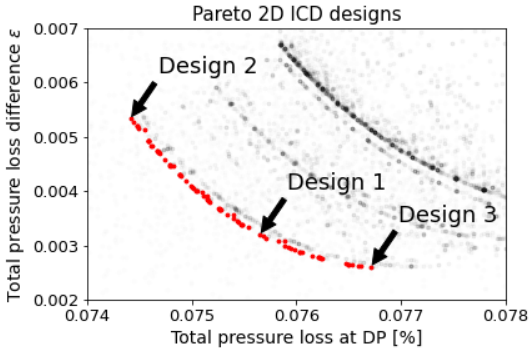

(b) Three designs of the loss objective criterion.

Figure 4.14: Pareto 2D plot for the designs from evolutionary algorithm. In the figure the designs that both fulfilled and violated the criterion are shown, as well as the designs that create the pareto front.

From the Pareto front, the three designs are tabulated for the design parameter outcome and response values given by the algorithm, see table 4.6.

Table 4.6: Tabulated data for the Pareto designs in the evolutionary algorithm optimization of the ICD.

Design parameters			
	Design 1	**Design 2**	**Design 3**
P1 global modification at Hub [mm]	3.804	3.803	3.818
P1 global modification at Shroud [mm]	-9.813	-9.813	-9.806
P2 global modification at Hub [mm]	4.989	4.989	4.989
P2 global modification at Shroud [mm]	-1.479	-1.479	-1.485
Max thickness location at 12.5% span [%]	-9.908	9.908	-9.908
Max thickness location at 50% span [%]	-5.171	-9.888	-1.289
Max thickness location at 87.5% span [%]	-2.248	-2.248	-2.248
Sweep angle at 12.5% span [deg]	-1.62959	-1.62918	-1.62988
Response values			
	Design 1	**Design 2**	**Design 3**
Separation surface area at DP $[m^2]$	0.002999	0.002998	0.002998
Separation surface area at NS $[m^2]$	0.002615	0.002615	0.002615
Outlet swirl angle at DP [deg]	0.009937	0.009943	0.009941
Outlet swirl angle at NS [deg]	0.922513	0.920465	0.932881
P0 loss difference ϵ	0.003201	0.005335	0.002609
P0 loss at DP [%]	0.075652	0.074414	0.076714

Between the three designs it can be noted that the parameter output values for P1 and P2 at both hub and shroud are given values within a very small range. The largest difference for the designs are for the maximum thickness location, although this parameter is not the most affecting parameter on the objective function of minimizing total pressure.

4.3.1 Aerodynamic analysis

From the Pareto designs the three designs was imported into CFX and run at both design point and off-design in order to analyze the aerodynamic performance. The comparison between designs were made by analyzing the isosurface of negative axial velocity and wall shear stress. Figures for isosurface and wall shear stress at design point for the designs are shown in appendix A. The largest affect of the designs are seen for the wall shear stress at off-design condition in figure 4.15 where the contour is shown for the wall shear stress in the range of 0 to 5 Pa as to see local separation tendencies. At design point the wall shear stress do not show this tendency, see figure A.2. The hub-corner close to trailing edge show that the flow is close to separation. The negative axial velocities do not show any tendency of reversed flow for either the design point or off-design point seen in figures A.1 and 4.16 .

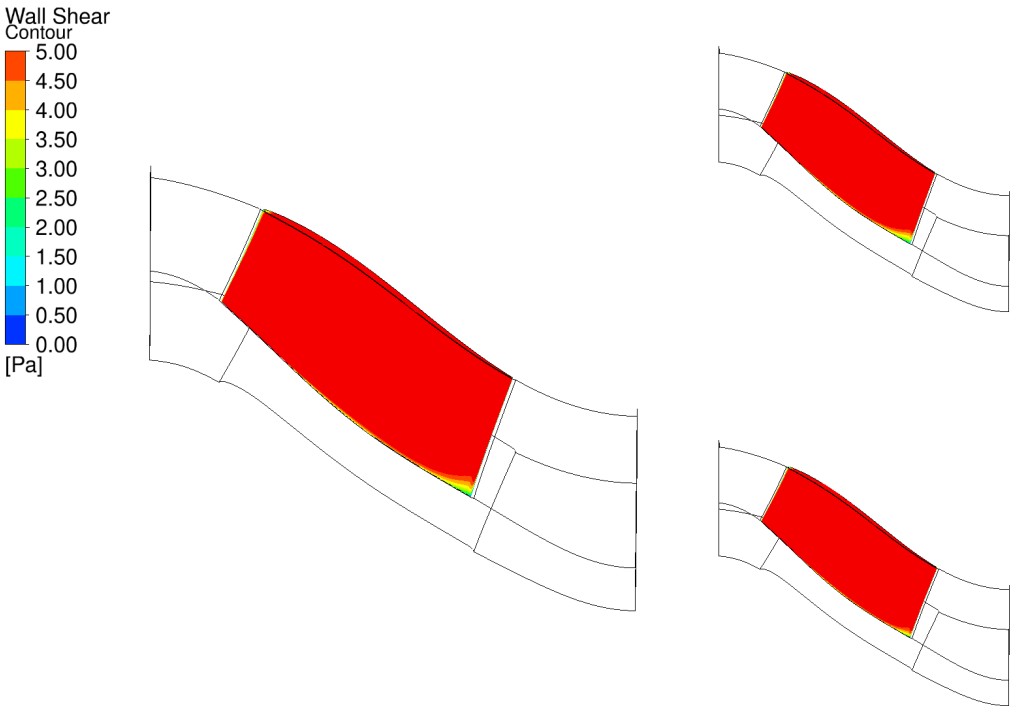

Figure 4.15: Contour plots of wall shear stress for the three ICD designs at off-design point from the Pareto front in the EA optimization. Design 1 is in the left most figure, following design 2 and design 3 in the top and bottom right figures respectively.

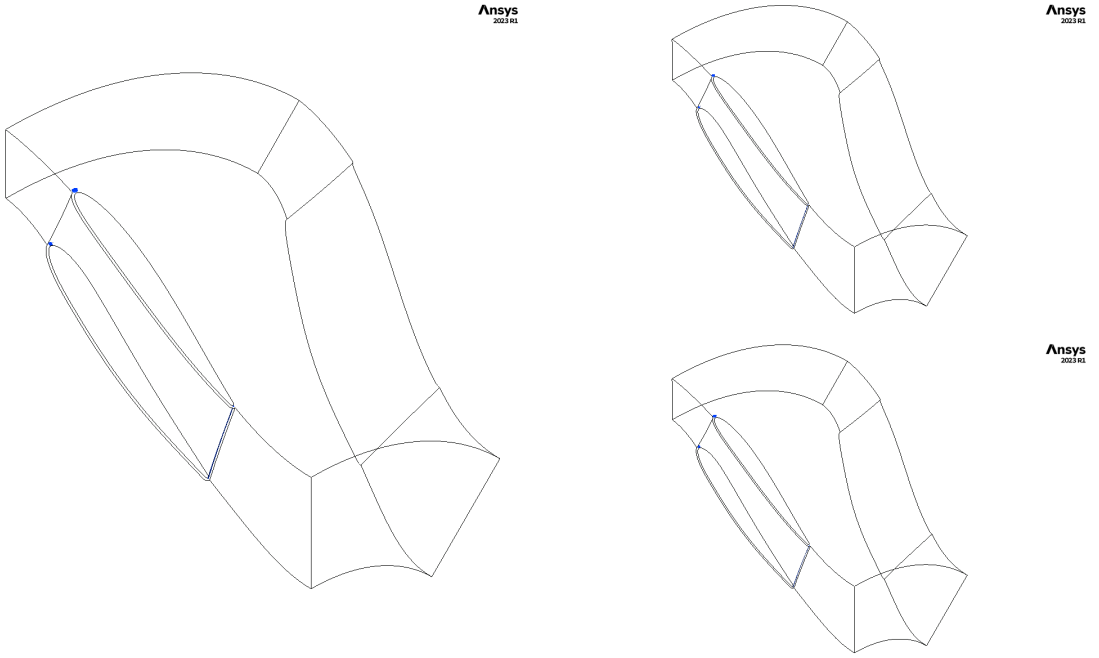

Figure 4.16: Isosurface for velocity of -0.01 m/s showing for the three ICD designs at off-design point from the Pareto front in the EA optimization. Design 1 is in the left most figure, following design 2 and design 3 in the top and bottom right figures respectively.

Total pressure loss for all three designs at design and off-design point is shown in figure 4.17. The largest difference, although very small, is seen for design 3 compared to the two other designs. Design 1 and 2 show very similar outcome in total pressure loss. Given that the ICD is a low-speed rig, the total pressure loss are shown to generate very low losses when evaluating the total pressure loss normalized with the inlet total pressure.

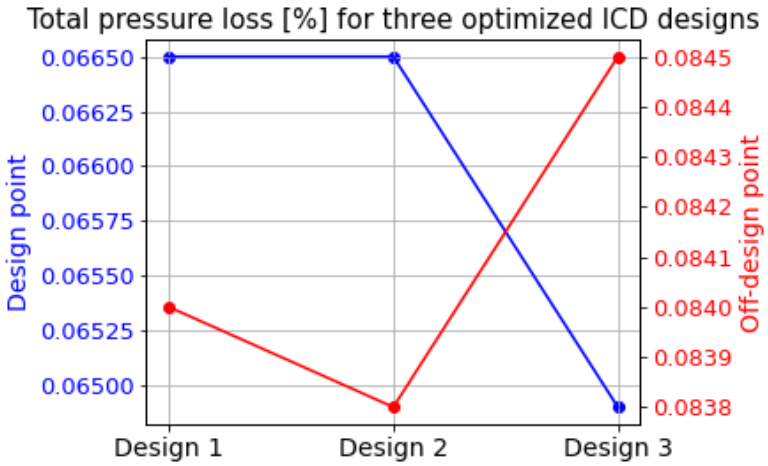

Figure 4.17: Total pressure loss for the three Pareto designs of the ICD.

The total pressure loss evaluated for the normalized values with inlet total pressure

shows very small loss differences, whereas the total pressure loss normalized with inlet dynamic pressure, ω, are presented in table 4.7. Evaluating for ω is useful when comparing performance with other ICD rigs as the inlet flow speeds in the rig might differ. Here it is clear that the pressure losses ω show higher results, varying between 3.40 to 5.06%.

Table 4.7: Total pressure loss ω, normalized with inlet dynamic pressure, tabulated for the three ICD pareto designs.

Total pressure loss ω [%]			
	Design 1	**Design 2**	**Design 3**
Total pressure loss at DP	3.42	3.40	3.34
Total pressure loss at NS	5.02	5.01	5.06

4.4 Final design

From the aerodynamic analysis of the three designs from the Pareto front in the previous section for the total pressure loss and the wall shear stress, ICD design 1 was chosen. The reasoning is that the total pressure increases at off-design point for design 3 and that there were minor differences between design 1 and 2. Shown in figure 4.18 the endwalls are shown for the optimized design and the baseline design. From the optimization it was found that a smaller gaspath contributed to minimizing total pressure loss.

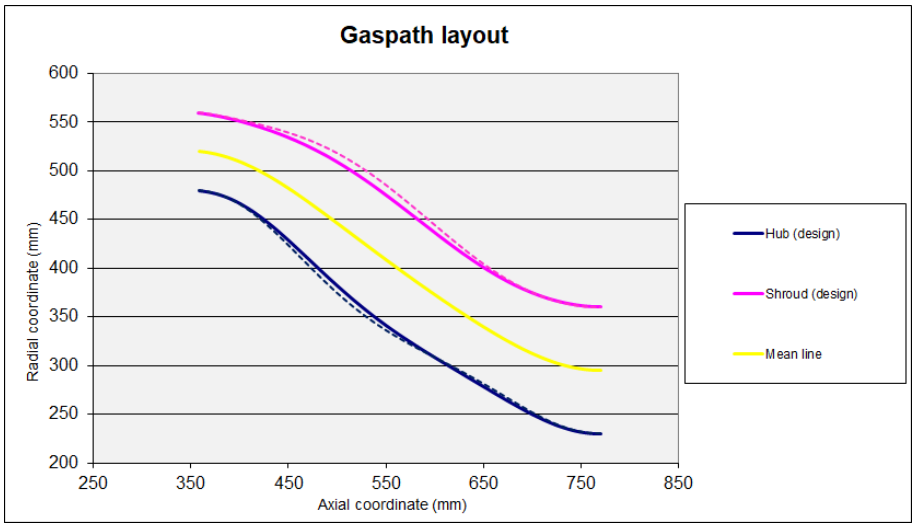

Figure 4.18: ICD endwall contours of the gaspath with the optimized design (thick line plot) and the baseline design (dashed plot).

The vane design at the three different spans are shown in figure 4.19. While the design changes are very small, the figure shows how the maximum thickness is moved closer toward the leading edge.

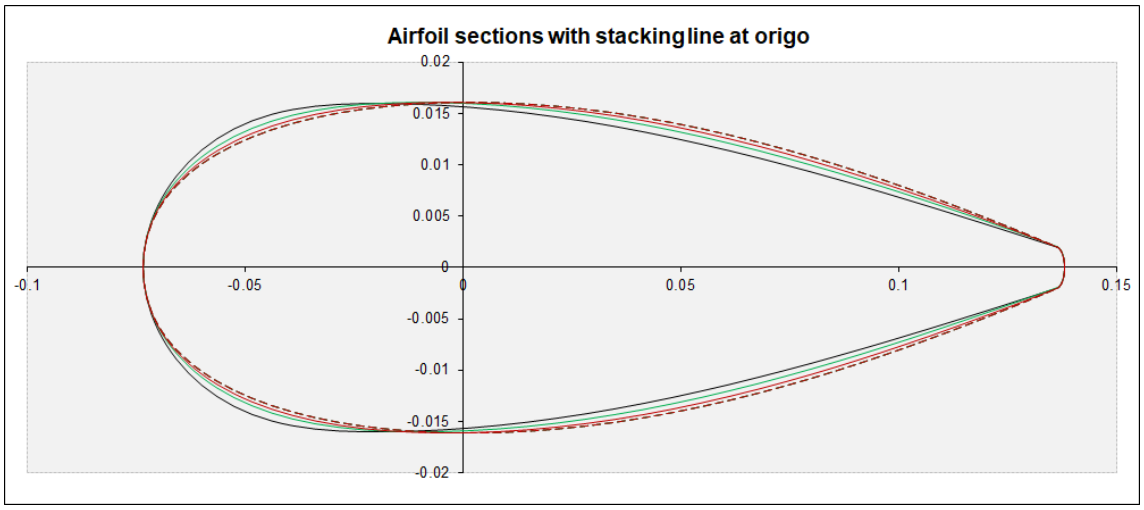

Figure 4.19: ICD airfoil at 12.5% span (black plots), 50% span (green plots) and 87.5% span (red plots) for the baseline design. The dashed line plots show the airfoils for the baseline design and the solid lines show the optimized airfoil design

Comparison between the baseline and the chosen optimized design was made for the outlet swirl angle profiles, seen in figure 4.20. The ICD optimized design at off-design point shows larger outlet swirl angles close to the hub, in figure 4.20. This could have been taken into account in the criteria when optimizing the ICD, where the maximum outlet swirl angle could be set for a limit or constraint.

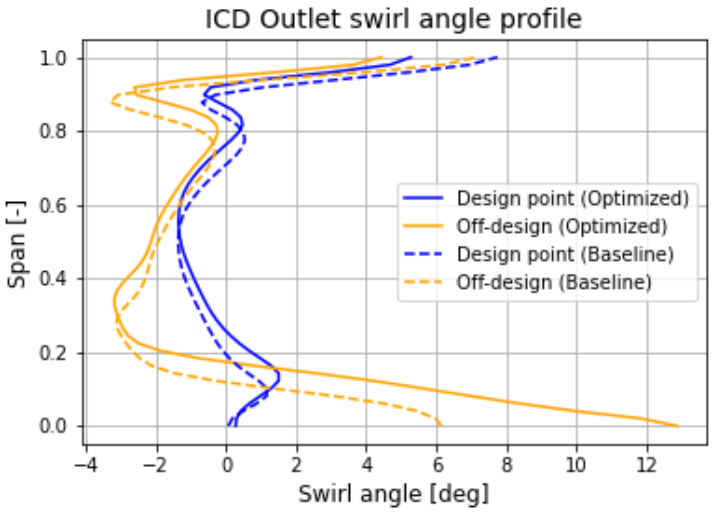

Figure 4.20: Swirl angle profiles for the baseline and optimized design of the ICD at design point and off-design point.

The total pressure loss between the two designs are shown in table 4.8.

Table 4.8: Total pressure loss for the ICD baseline and optimized designs at design and off-design point.

	Baseline	**Optimized**	**Difference**
Design point	0.083%	0.067%	-19.69%
Off-design point	0.115%	0.084%	-26.77%

A comparison of the optimized design with the predicted response on the total pressure loss at design point and the difference in total pressure loss between flow conditions is seen in table 4.9.

Table 4.9: Comparison between the predicted total pressure loss from the MOP response surface for the optimized ICD with the results from CFD.

	Response surface	**Optimized**	**Difference**
Total pressure loss at DP	0.076%	0.067%	-12.15%
Total pressure loss difference ϵ	0.0032	0.0002	-94.53%

4.4.1 Incorporating ICD with compressor stages

Including the optimized ICD design into the whole compressor system the ICD is analyzed further. Figure 4.21 for design point and A.3 in appendix A show isosurfaces of negative axial velocity. When comparing the designs it can be seen that the separation that occured close to the vane-hub corner in the old design is improved with the optimized design at both design and off-design conditions. The wall shear stress along the blade surface is shown in figure 4.22 for design point and in appendix X in figure A.4 for off-design point. In the figures the difference in wall shear stress can be seen where the new design shows very low tendency for separating the flow.

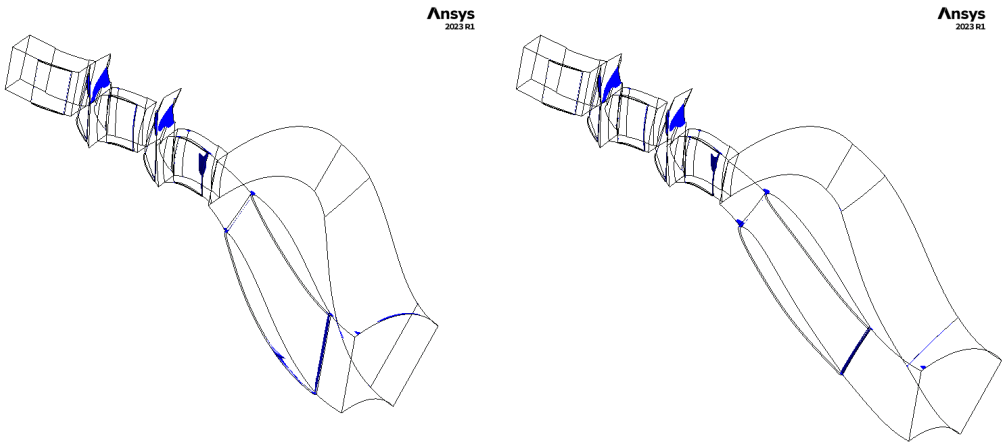

Figure 4.21: Whole compressor system with the old and optimized design included in the left and right figures respectively. Isosurface of blue color shows negative axial velocity of -0.1 m/s at design point.

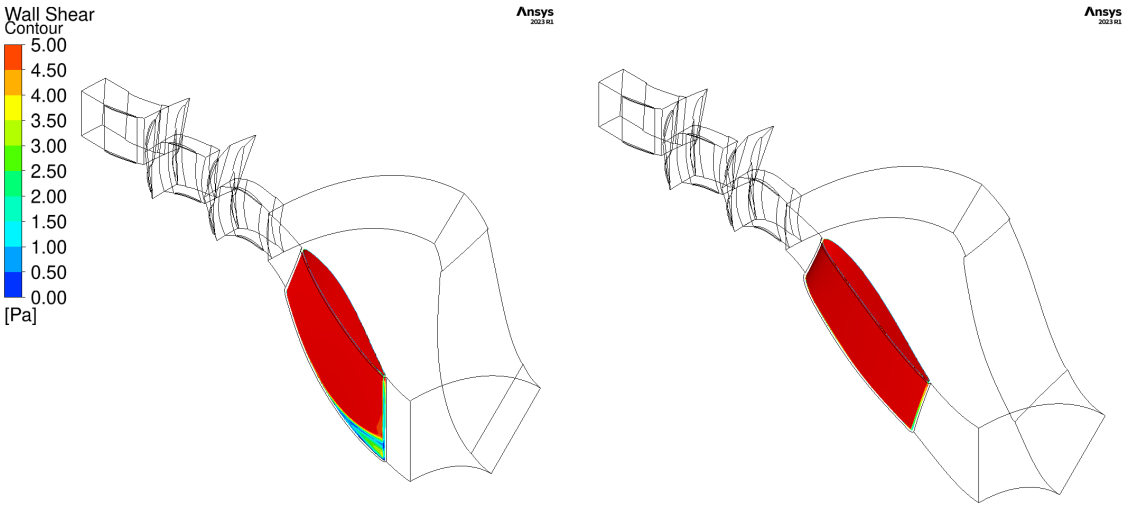

Figure 4.22: Whole compressor system with the old and optimized design included in the left and right figures respectively. Contour of wall shear stress is shown at design point.

Results for outlet swirl angle, total pressure and total temperature profiles are shown in figures 4.23, 4.24 and 4.25.

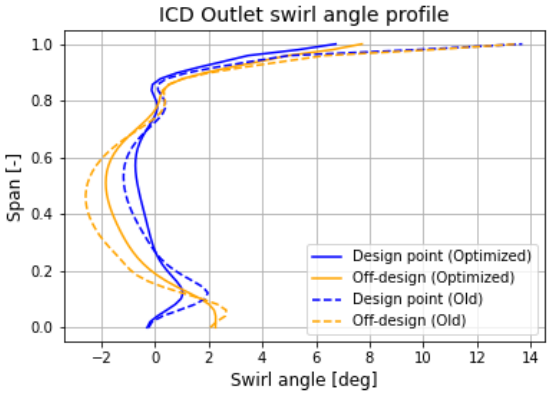

Figure 4.23: Compressor stages with the optimized ICD design included. The figure shows outlet swirl angle profiles.

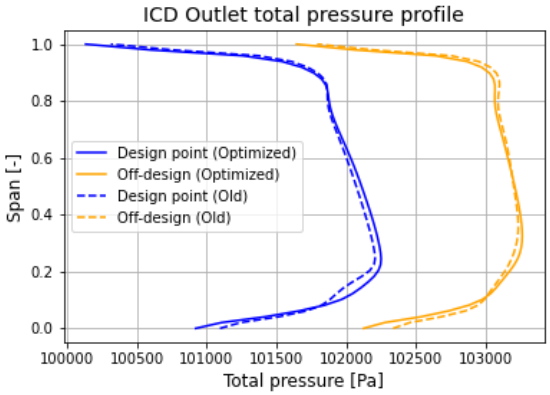

Figure 4.24: Compressor stages with the optimized ICD design included. The figure shows outlet total pressure profiles.

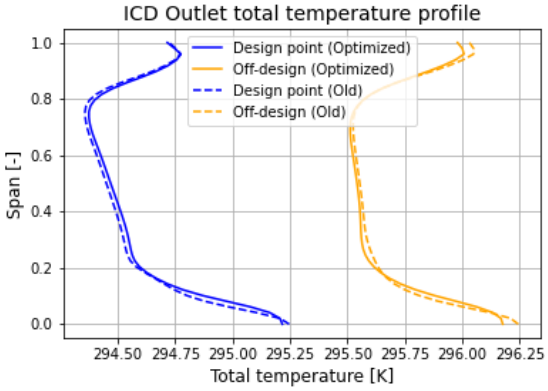

Figure 4.25: Compressor stages with the optimized ICD design included. The figure shows outlet total temperature profiles.

The total pressure loss and average outlet swirl angle for the original and optimized design are presented in table 4.10, for both design and off-design flow conditions. The total pressure loss at design point has not been greatly affected for the optimized design compared to the original, while for the off-design conditions, the total pressure loss shows a large reduction. The average swirl angle is also seen to increase at off-design point, however it increased with about one degree and the average outlet swirl angle is kept below one degree at the outlet, so the difference between the designs is not concerning.

Table 4.10: Results for the total pressure loss and average outlet swirl angle for the original ICD design and the optimized design, at both design and off-design condition.

	Original	**Optimized**	**Difference**
Average outlet swirl at DP	0.30	0.03	-0.27
Average outlet swirl at NS	-0.16	0.86	+1.02
Total pressure loss at DP	0.069%	0.067%	-2.78%
Total pressure loss at NS	0.133%	0.084%	-36.98%

5
TEC design

Methods for designing the baseline design, optimizing and analyzing the TEC design is described in this section.

5.1 Method

The TEC endwall corner points for axial and radial inlet and outlet coordinates are given in table 5.1 and will be the starting points for creating the endwall hub and shroud contours.

Table 5.1: TEC endwall corner points

	Hub	**Shroud**
Radial inlet coordinate [mm]	326.0	603.6
Radial outlet coordinate [mm]	325.0	603.7
Axial inlet coordinate [mm]	298.8	301.3
Axial outlet coordinate [mm]	733.8	733.8

The TEC OGV leading edge is positioned at two axial chord lengths (based on the upstream turbine rotor), downstream of the turbine. The axial chord length and maximum thickness of the vanes at spans 12.5%, 50% and 87.5% are calculated by setting the solidity and maximum thickness over axial chord τ. The vane geometry is designed towards boundary conditions at inlet to match the incoming flow from the LPT and matching the flow at the outlet for close to zero degree swirl angle. The design parameters were determined by setting parameters at hub, mid and shroud spans (12.5%, 50% and 87.5%) of leading and trailing edge camber angles and their first and second derivatives and radius of leading edge, by running the design through the 2D solver. Remaining spans are interpolated from the three spans for the same geometrical parameters. The leading edge are chosen such that a negative incidence angle occurs, as to create a design that can handle off-design points well, for high inlet angles. Numbers of struts are given to be 12 and the airfoils at each span is stacked in a straight line at maximum thickness.

Aerodynamic performance is then analyzed for the TEC at design and off-design flow conditions throught the 3D CUDA solver as to assure that the flow does not separate and keeps an outlet flow angle close to zero for maximum thrust. In the analysis the static pressure coefficient plot is analyzed to see that the design has a suction peak that matches the location of the maximum thickness. A Stratford

shape of the static pressure at the suction side, going from maximum suction point towards trailing edge, is sought as to keep the flow diffusion minimal. Separation is monitored by looking at the Stratford criterion plot, where a Stratford coefficient above -0.2 has been considered the limit for separation not to occur. Separation is also checked by looking at the wall shear stress along the vane surface at the pressure and suction side, here the values has been assured to not be close to zero and a value above wall shear stress above 5 had bee considered for no indication.

5.1.1 Boundary conditions

The boundary conditions at the design point is represented by the top-of-climb point for the aircraft, and end-of-runway (EOR) which is here denoted as the off-design condition. The inlet swirl angle profile, inlet total pressure profile and inlet total temperature profile is plotted at these two flow conditions, seen in figures 5.1, 5.2 and 5.3. It should be noted that the off-design boundary condition at EOR were provided after the TEC design and analysis were evaluated and hence off-design points of only changing the inlet swirl angle profile by adding and subtracting 10 degrees has been used as a robust measure. The boundary conditions at EOR was used in the acoustic study.

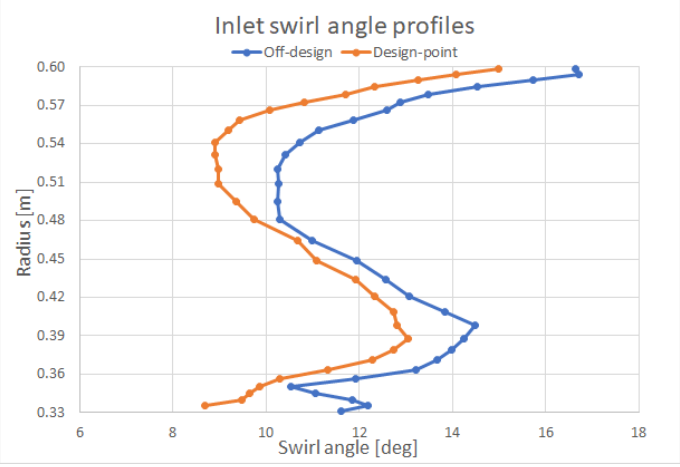

Figure 5.1: Inlet swirl angle profile for the TEC at design and off-design points.

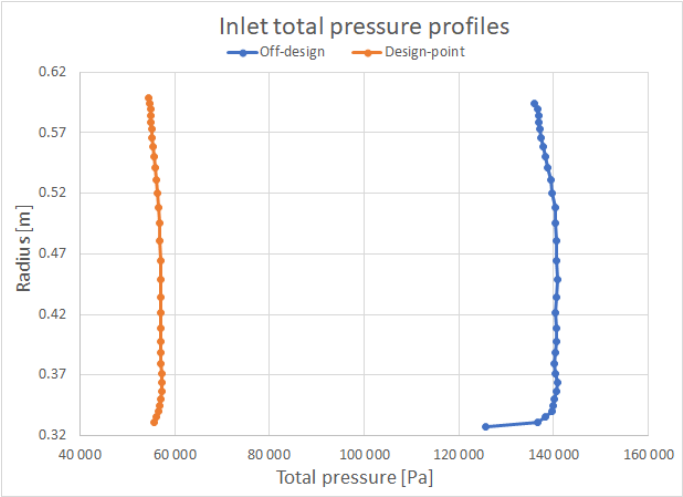

Figure 5.2: Inlet total pressure profile for the TEC at design and off-design points.

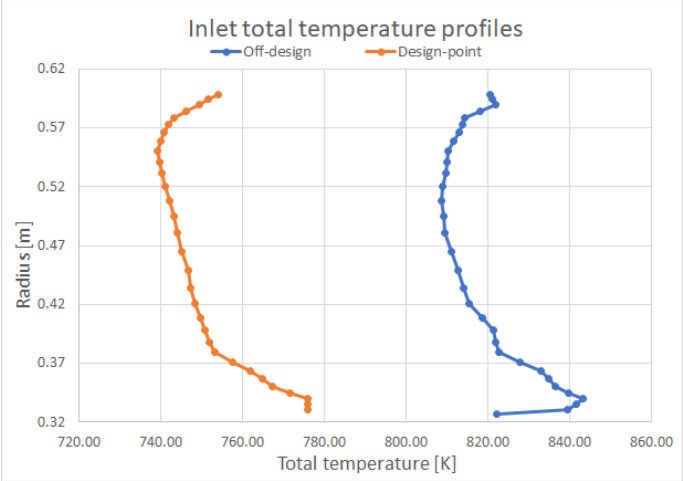

Figure 5.3: Inlet total temperature for the TEC at design and off-design points.

5.2 Design

Designing the TEC starts by defining the gaspath endwalls which is drawn from radial and axial inlet and outlet coordinates. Following the baseline of the endwalls, the vane geometry is designed towards inlet boundary conditions and targeted outputs. The off-design conditions are evaluated with robust boundary conditions by keeping the same flow proprties at design point while changing the inlet swirl angle profile by subtracting and adding 10 degrees, which will be denoted by two off-design points of m10 and p10 respectively. This robust measure was used as to evaluate the design for varying flow conditions at the inlet.

5.2.1 Establishing a baseline design

Gaspath endwall maximum perturbations for the baseline design is shown in table 5.2 and the resulting contour is shown in figure 5.4. The gaspath is increasing in meridional area as to increase diffusion since a straight gaspath showed separations at the hub and shroud trailing edge corner. Increased diffusion around the mid-sections of the vanes decreases the acceleration at the maximum thickness location and thus decreases risk of boundary layer separation. To avoid flow separation in the rear part of the vane, the flow area is increased up to the peak suction point of the vanes, and subsequently decreased. The decreasing passage area aft of peak suction contribute to a less severe adverse pressure gradient, reducing the risk for flow separation.

Table 5.2: Start values for endwall parameters for the TEC.

	Hub (12.5%)	**Shroud (87.5%)**
P1 [mm]	-14	14

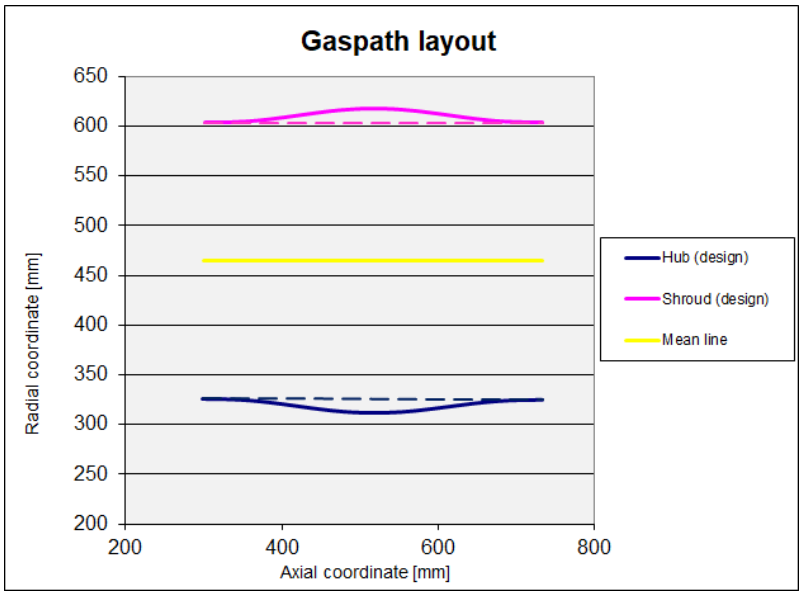

Figure 5.4: Gaspath endwalls plot for the start design of the TEC. The dashed lines show the original endwall contour and the consequetive lines show the start design of the endwalls for the hub and shroud.

5.2.2 Creating baseline design

The vane design started by calculating the axial chord length and maximum thickness from solidity and maximum thickness over axial chord τ at three spans, see table 5.3.

Table 5.3: TEC calculated axial chord length and maximum thickness from solidity and maximum thickness to axial chord ratio τ.

	Hub (12.5%)	**Mid (50%)**	**Shroud (87.5%)**
Solidity	1.17	0.87	0.71
Max thickness/axial chord τ	0.15	0.15	0.15
Axial chord [mm]	203	212	222
Maximum thickness [mm]	30.5	31.8	33.4

During the design process, aerodynamic analysis was performed as to assure that separation at the vane or endwall surfaces does not occur and that the outlet radial swirl angles maintained a profile close to zero. Geometrical parameters at the three spans are shown in table 5.4 for a design that show aerodynamic performance for both design-point and off design-point.

Table 5.4: Start design of the TEC vanes at 12.5%, 50% and 87.5% span.

Span position of section	**12.5%**	**50.0%**	**87.5%**
Axial Chord [mm]	203	212	222
LE camber angle [deg]	11.0	15.0	20.4
TE camber angle [deg]	-1.60	-1.80	-0.80
LE camber-angle / ds	-0.40	-0.50	-0.32
Max thickness [mm]	30.5	31.8	33.4
Max thickness location [%]	35.9	32.9	30.2
LE thickness [mm]	5.00	5.00	5.00
Front wedge angle adjust [deg]	-7.32	-5.50	-5.07
Front thickness adjust	-2.00	-2.00	-2.20
Max thickness curvature	-2.70	-2.80	-3.02
TE wedge angle adjust [deg]	-4.00	-4.00	-4.02
Rear thickness adjust	1.00	1.00	1.00
TE thickness [mm]	3.00	3.00	3.00

The vane geometry for the TEC is shown in figure 5.5, note the difference of the scales in each direction.

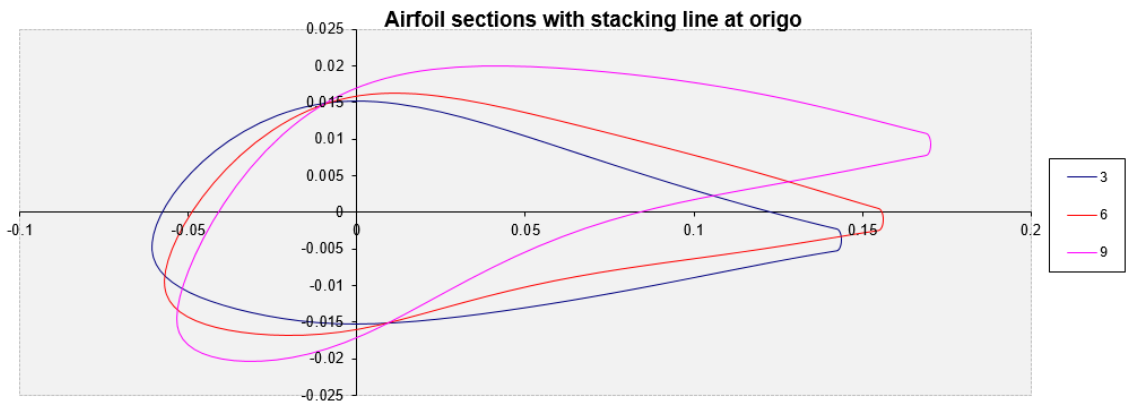

Figure 5.5: Vane geometry at 12.5% (3), 50% (6) and 87.5% (9). Plot view is in the stacking line at orgin of the plot.

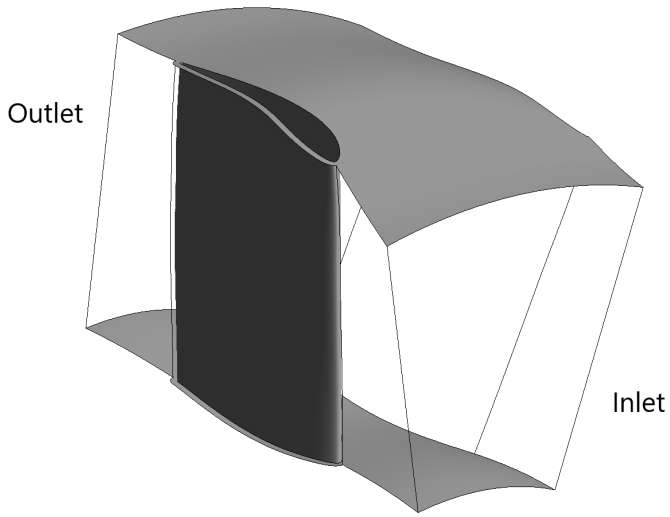

Figure 5.6: TEC start design isoparametric view.

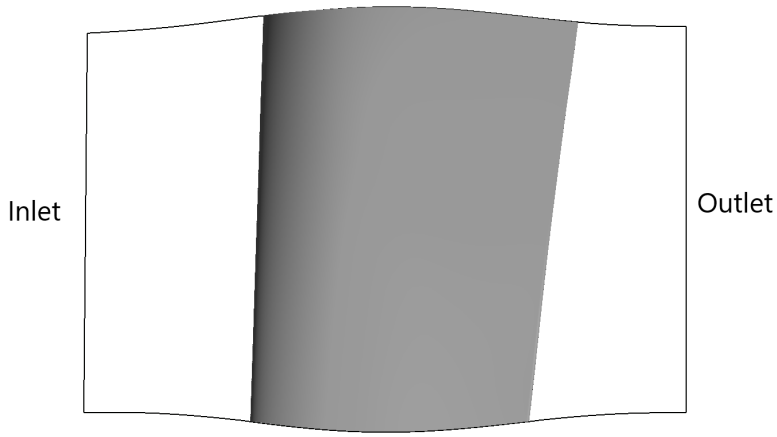

Figure 5.7: TEC baseline design showing a side view of the vane and endwall profiles. To the left is the inlet and to the right is the outlet.

Aerodynamic performance of the TEC is tracked by looking at the static pressure coefficient plot to see where the suction peak occurs. Ideally this point should be as close to the maximum thickness location as possible and have a strong acceleration just up to that point to then decelerate and shape a Stratford shape where the flow slows down, seen in figure 5.8.

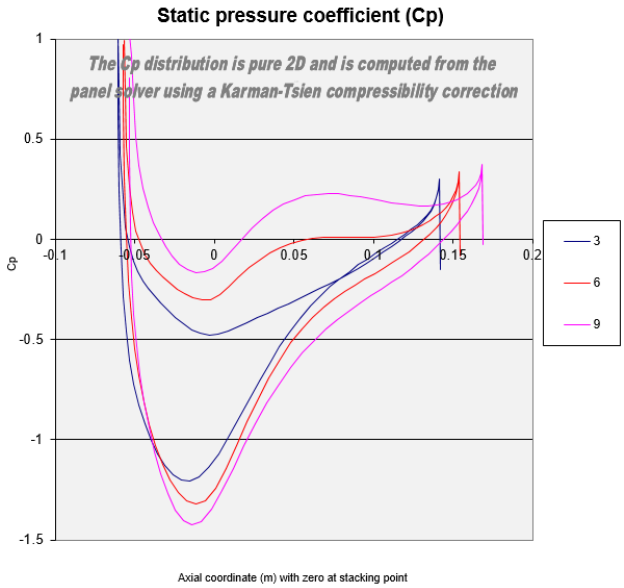

Figure 5.8: Static pressure coefficient plot for vane spans at 12.5% (3), 50% (6) and 87.5% (9)

In order to visualize the endwall affect on the diffusion of the flow along the vane surface, a contour plot of static pressure is shown in figure 5.9. The acceleration of the flow, seen for low static pressure, can be seen close to the leading edge and down stream towards the location of maximum thickness. The flow is then decelerated and close to the endwalls the static pressure increases further upstream compared to the mid span flow section.

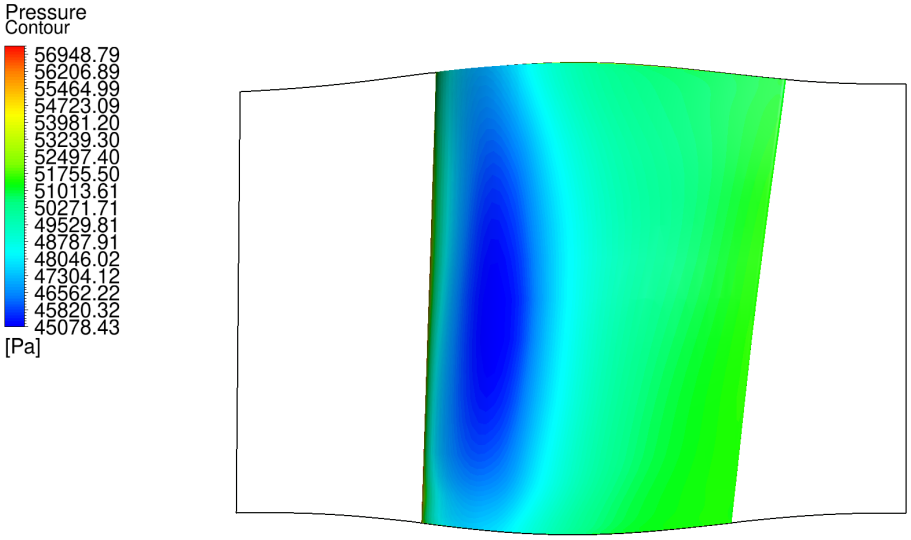

Figure 5.9: Contour plot of the static pressure along the suction side surface of the TEC baseline design. To the right is the inlet of the TEC and to the left is the outlet.

The TEC is analyzed for the Stratford criterion which indicates where the flow is prone to separate along the vane surface, see figure 5.10. Although the separation limit is close to zero, the 2D solver for which calculated the Stratford criterion does not account for 3D effects and usually a guideline of a Stratford coefficient of -0.2 has been used for limit.

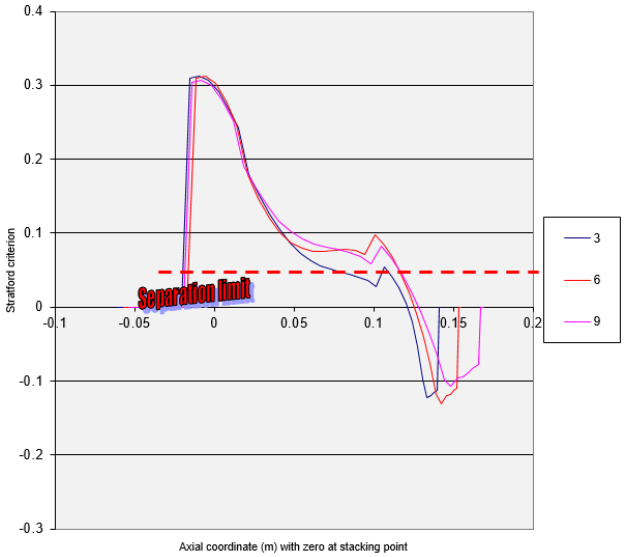

Figure 5.10: Stratford criterion plot for vane spans at 12.5% (3), 50% (6) and 87.5% (9)

The wall shear stress at both suction and pressure side shows no indication on separation, see figures 5.11 and 5.12. A slight tendency can be seen in the design process, although with an increase in meridional area by changing the endwalls, the wall shear stress increased.

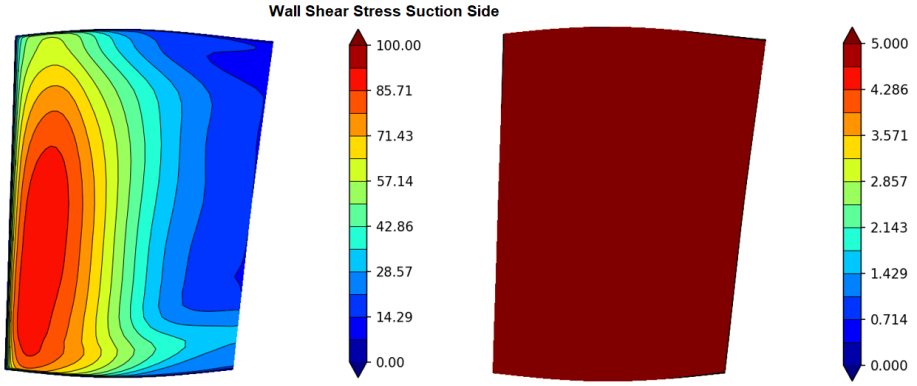

Figure 5.11: Wall shear stress at the suction side of the vane. Left figure shows the wall shear contour plot in the range of 0-100 Pa and the right figure shows the range of 0-5 Pa.

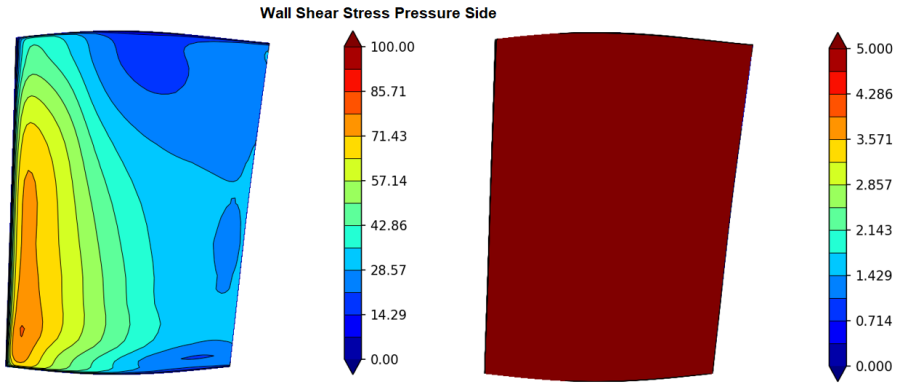

Figure 5.12: Wall shear stress at the pressure side of the vane. Left figure shows the wall shear contour plot in the range of 0-100 Pa and the right figure shows the range of 0-5 Pa.

5.3 Mesh study

In the current section two different approaches are used to create meshes for unrefined and refined boundary layer meshes in order to get a mesh which applies wall functions and low-Re models respectively when using turbulence models of $k-\epsilon$ and $k-\omega$. Deciding the mesh size for each mesh of which produces independent CFD results is done for a wall function mesh and low-Re number mesh. All meshes are run for the same static pressure at the outlet.

5.3.1 Wall function mesh

A mesh study for applying wall functions were made for five different meshes. Values of y^+ at the walls needs to be within the range for wall functions (described in section 2.7) and parameters for average swirl at the outlet, total pressure loss and mass flow at the inlet are monitored. From the start mesh (Medium), a coarse mesh (Coarse) and three fine meshes are generated (fine and very fine), see table 5.5. The coarse mesh is constructed for half the starting mesh size, while the fine meshes are of double and four times the mesh size.

Table 5.5: Mesh study for wall functions mesh using radial profile boundary conditions at inlet.

	Grid cells	y^+	α **[degrees]**	**p0 loss**	$\dot{m}$ **[kg/s]**	**Max M**
Coarse	321k	77.89	0.522239	0.002839	39.934400	0.572942
Medium	631k	54.39	0.379734	0.002268	40.096500	0.630830
Fine	1 270k	50.85	0.366207	0.002212	40.104600	0.642386
Very fine	2 525k	49.15	0.346521	0.002175	40.110700	0.646999

By having all nodes in the coarse mesh less than 10 meshing nodes, the wall models will be applied, described in method/wall functions.

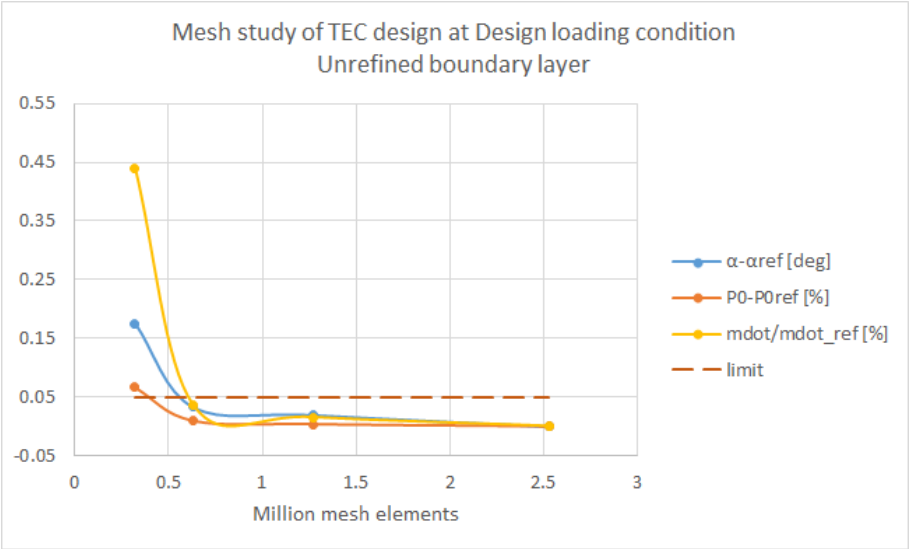

Figure 5.13: Mesh study plot of the unrefined TEC meshes.

The mesh that was chosen to continue with was the medium mesh, since that mesh produces converged results. A finer mesh would not show any larger difference on the results, and the mesh is considered converged when reaching blow 5% tolerance.

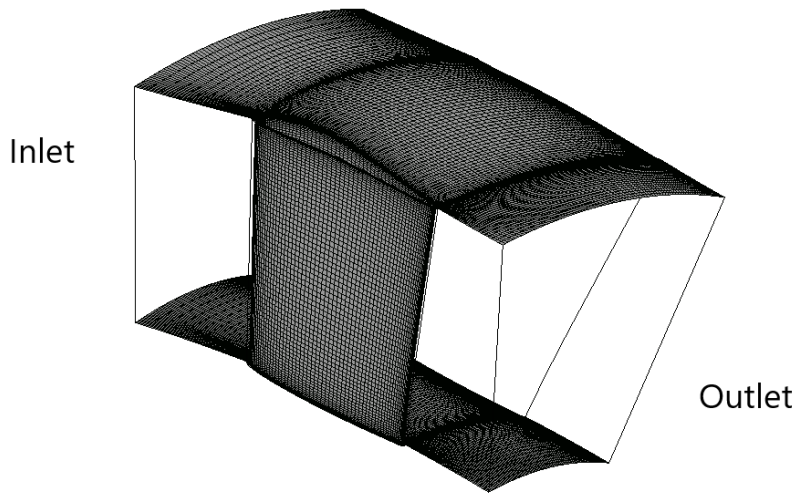

Figure 5.14: Isometric view of the unrefined mesh for the TEC.

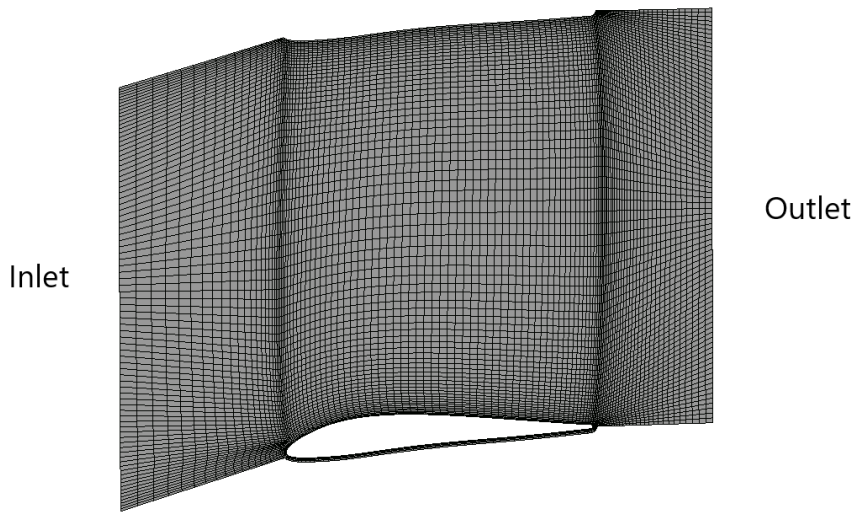

Figure 5.15: Top view of the unrefined mesh at the shroud of the TEC.

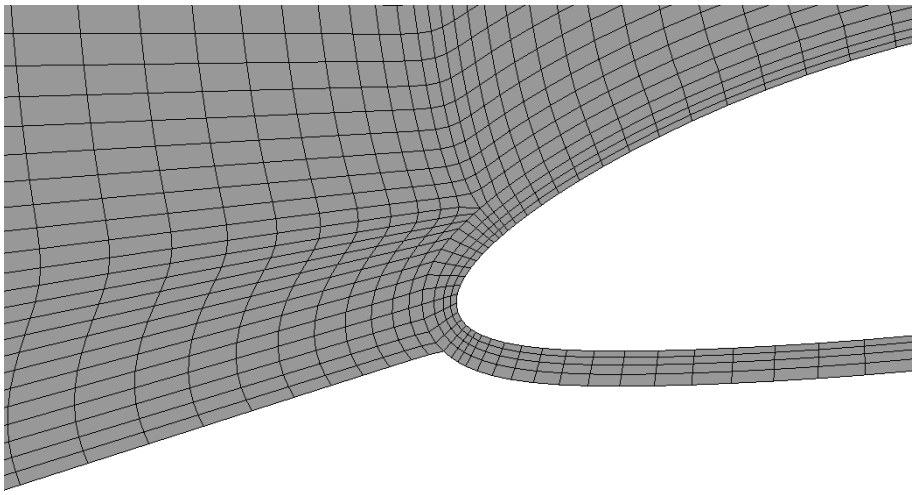

Figure 5.16: Zoom-in view of the leading edge at the shroud of the TEC.

5.3.2 Low-Re mesh

In order to create a mesh with a refined boundary layer, a starting mesh is constructed with 12 nodes in the boundary layer mesh zone in order to get a low-Re mesh. The grid spacing normal to the wall for the first cell at the wall is found for a mesh that gives a y^+ value less than 1. This gives the mesh of grid size 714 189 elements and a first cell grid spacing of 5e-10 m and gives a y^+ value of 0.6503.

A mesh study is then made for the low-Re mesh to get independent mesh results. The mesh sizes for the low-Re meshes are shown in table 5.6.

Table 5.6: Mesh study results for low-Re meshes using radial profile boundary conditions at inlet.

	Grid cells	y^+	α **[deg]**	**p0 loss**	$\dot{m}$ **[kg/s]**	**Max M**
Coarse	238k	0.915752	-0.566337	0.002595	39.9208	0.590636
Medium	485k	0.931807	-0.563135	0.002464	39.9608	0.59165
Fine	970k	0.877761	-0.537235	0.002405	39.9776	0.59222
Very fine	1 941k	0.812544	-0.537378	0.002369	39.9883	0.592523
Ultra fine	2 916k	0.807288	-0.538105	0.002352	39.9901	0.592626

The mesh chosen to continue with from the refined boundary layer meshes is the fine mesh, since it produces converged results for the output and the mesh has reached results blow 5% tolerance.

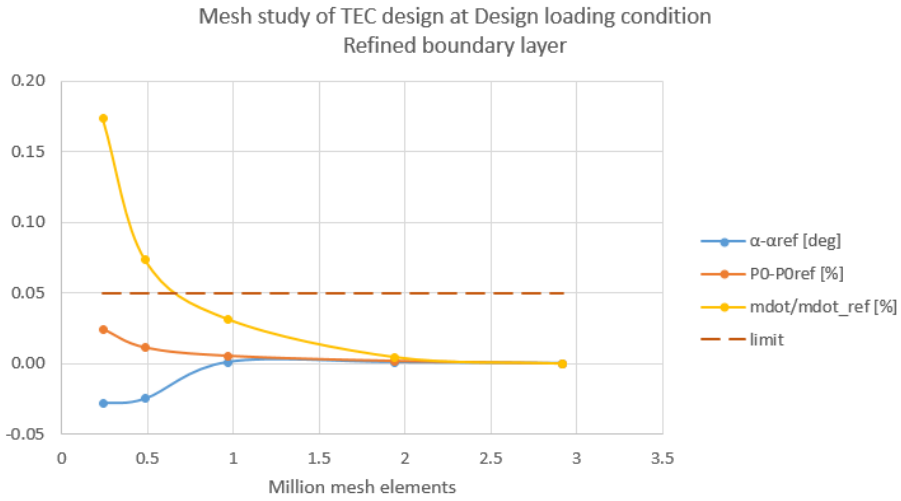

Figure 5.17: Mesh study plot of the refined TEC meshes.

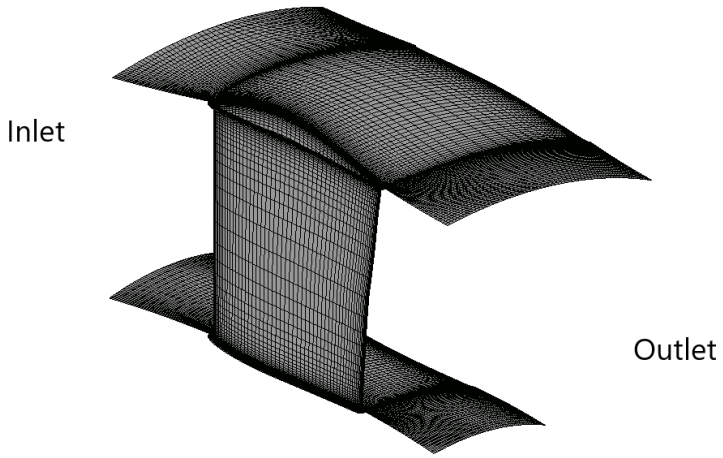

Figure 5.18: Isometric view of the refined mesh for the TEC.

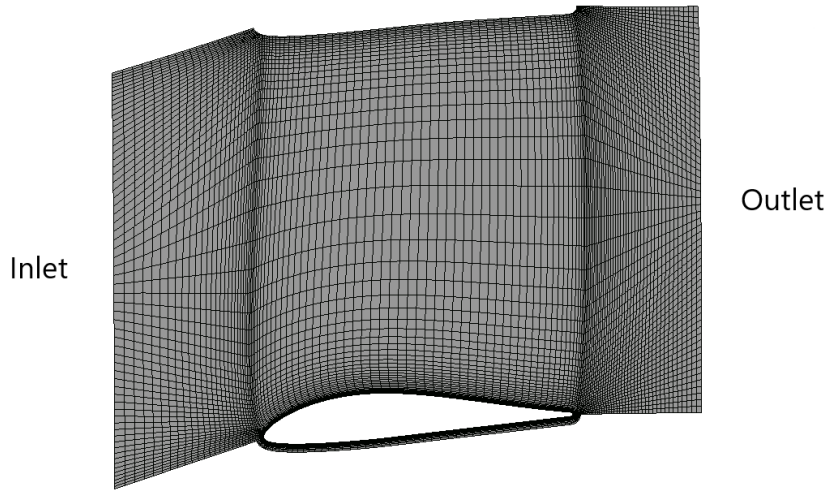

Figure 5.19: Top View of the refined mesh at the shroud of the TEC.

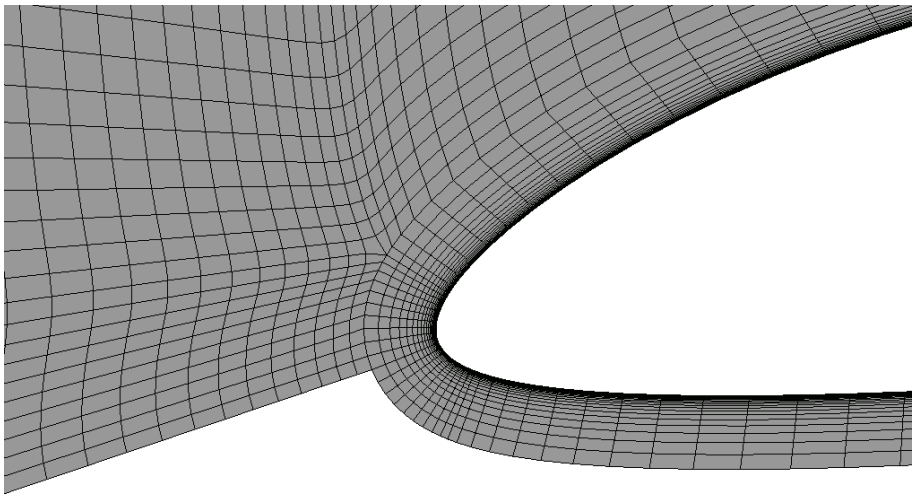

Figure 5.20: Zoom-in view of the leading edge at the shroud of the TEC.

5.4 TEC design optimized in OptiSLang

With the TEC design shown in the previous section, the parameters varied in the DOE scheme are chosen according to table 5.7. A total of 6 parameters were varied whereas 56 designs were generated, by doubling the calculated number of designs with equation (3.7). For the optimization process double the amount of designs were generated to construct a second order polynomial from the response to assure a response surface design space.

Table 5.7: Interval for values for parameters from DOE for endwall splines of maximum perturbation, leading and trailing edge camber angles and maximum thickness location.

	Hub (12.5%)	**mid (50%)**	**Shroud (87.5%)**
P1 [mm]	+/- 5	-	+/- 5
LE θ [deg]	+/- 5	+/- 5	+/- 5
t_{loc}/C_{ax} [%]	+/- 2	+/- 2	+/- 2

With the DOE matrix and geometries generated, a MOP is created in OptiSLang. From the MOP the response surfaces for the objectives of minimizing total pressure loss at design point and total pressure loss ϵ is shown in figures 5.21a and 5.21b. The design parameters chosen for the response surface are the ones that have the greatest effect on the objective functions and constraints. For the TEC designs the figures show that the largest affects are for the P1 shroud endwall parameter and leading edge camber angle parameter at 50% span for minimizing total pressure loss at design point. For minimizing ϵ the parameters for leading edge camber angle at 87.5% span and max thickness location at 12.5% span were the most affecting ones.

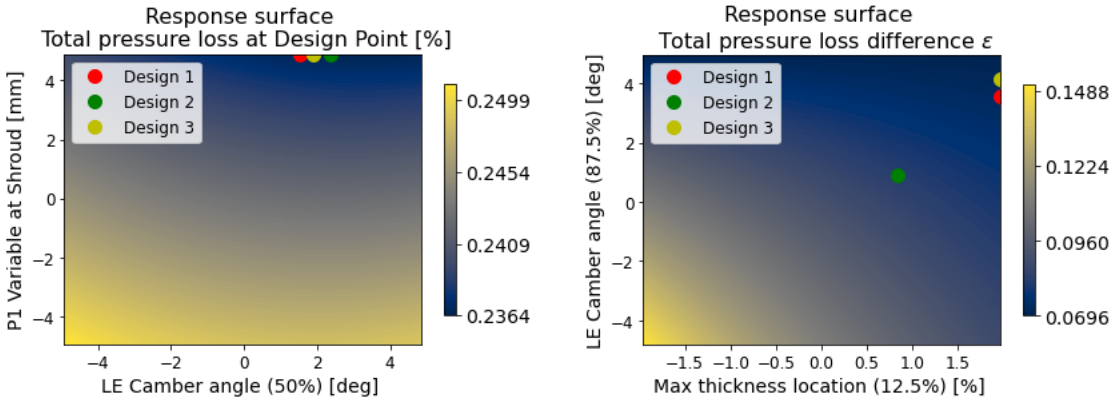

(a) Leading edge camber angle and P1 modification at shroud endwall.

(b) Leading edge camber angle and max thickness location.

Figure 5.21: Response surface contour plots for the TEC designs when running the DOE in the MOP in OptiSLang. Seen in the figures are also the designs which is chosen from the evolutionary algorithm optimization, described later in this section.

From the response surface and the designs from the MOP, criteria are set for the average outlet swirl angle and separation surface area at both design and the two off-design points. The criteria limits are determined by analyzing the output results from the DOE and finding the lowest values for the outputs. The criterion are then set and the objective functions for minimizing total pressure loss at design point and minimizing ϵ between the flow conditions are set.

The designs are then run with the evolutionary algorithm where the criteria in table 5.8 were set for the parameters after iterating the optimization for criteria that fulfill the wanted responses.

Table 5.8: Criterion for the evolutionary algorithm of the TEC DOE in OptiSLang, which are determined for the design point and the robust measured off-design points m10 and p10 for the inlet swirl angle profile.

Criteria for evolutionary algorithm	
Average outlet swirl at DP [deg]	<= 1
Average outlet swirl at m10 [deg]	<= 2
Average outlet swirl at p10 [deg]	<= 2
Separation surface area at DP $[m^2]$	<= 0.1
Separation surface area at m10 $[m^2]$	<= 0.1
Separation surface area at p10 $[m^2]$	<= 2
P0 loss at DP	MIN
P0 loss difference ϵ	MIN

From the evolutionary algorithm a Pareto 2D plot was generated for the designs, seen in figure 5.22. The optimized design given by the evolutionary algorithm is design 1, whereas for the extremities of the objective functions for low total pressure loss at design point a design is given as design 2 and for the low total pressure loss ϵ as the design 3. Seen in the figures for the response surfaces of the most affecting design parameters, figures 5.21a and 5.21b, the three design response values are shown in red, green and yellow. All designs show similar response for optimizing towards total pressure loss at design point, while for optimizing toward ϵ design 2 show lower design parameter values and response value than design 1 and 3.

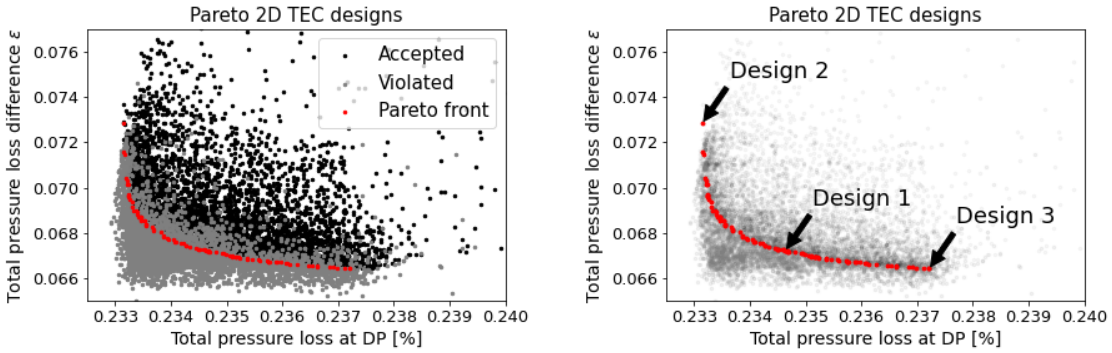

(a) Zoom in on the pareto front for fulfilled, violated, and pareto designs.

(b) Three designs of the loss objective criterion.

Figure 5.22: Pareto 2D plot for the designs from evolutionary algorithm. In the figure the designs that both fulfilled and violated the criterion are shown, as well as the designs that create the pareto front.

The optimized design chosen by the evolutionary algorithm is given by the changes from the baseline design with values given in table 5.9. The design parameters and response values are shown for each of the three chosen designs in the Pareto front, where the swirl angle is evaluated by area average at the outlet. Comparing the response values for the designs, it can be seen that the largest difference is shown for the leading camber angle at 12.5% and 87.5% span.

Table 5.9: Design parameters and response values for design 1, 2 and 3 from the Pareto front in the evolutionary algorithm. The outlet swirl angle is given for an area averaged value.

Design parameters			
	Design 1	**Design 2**	**Design 3**
P1 global modification at Shroud [mm]	4.89	4.89	4.89
P1 global modification at Hub [mm]	-4.95	-4.95	-4.95
Max thickness location at 87.5 % span [%]	-1.06%	-1.06%	-1.06%
Max thickness location at 50% span [%]	-1.06%	-1.06%	-1.06%
Max thickness location at 12.5% span [%]	1.97%	0.84%	1.97%
LE camber angle at 87.5% span [deg]	3.57	0.91	4.13
LE camber angle at 50% span [deg]	1.51	2.37	1.89
LE camber angle at 12.5% span [deg]	-1.07	2.54	-4.43
Response values			
	Design 1	**Design 2**	**Design 3**
Separation surface area at DP $[m^2]$	0.0626	0.0626	0.0616
Separation surface area at m10 $[m^2]$	0.0567	0.0563	0.0579
Separation surface area at p10 $[m^2]$	1.9254	1.9186	1.9099
Outlet swirl angle at DP [deg]	0.1194	0.1109	0.1598
Outlet swirl angle at m10 [deg]	1.8770	1.8739	1.9038
Outlet swirl angle at p10 [deg]	0.0019	0.0035	0.0004
P0 loss ϵ	0.0672	0.0728	0.0664
P0 loss at DP [%]	0.2346	0.2331	0.2372

When analyzing the separation for the three designs for boundary conditions at design point flow condition, it was noticed that the design for low total pressure loss at design point (design 2) showed somewhat higher separation close to the hub leading edge of the vane. The design for low total pressure loss ϵ (design 3) showed similar separation as the optimized design from the EA (design 1).

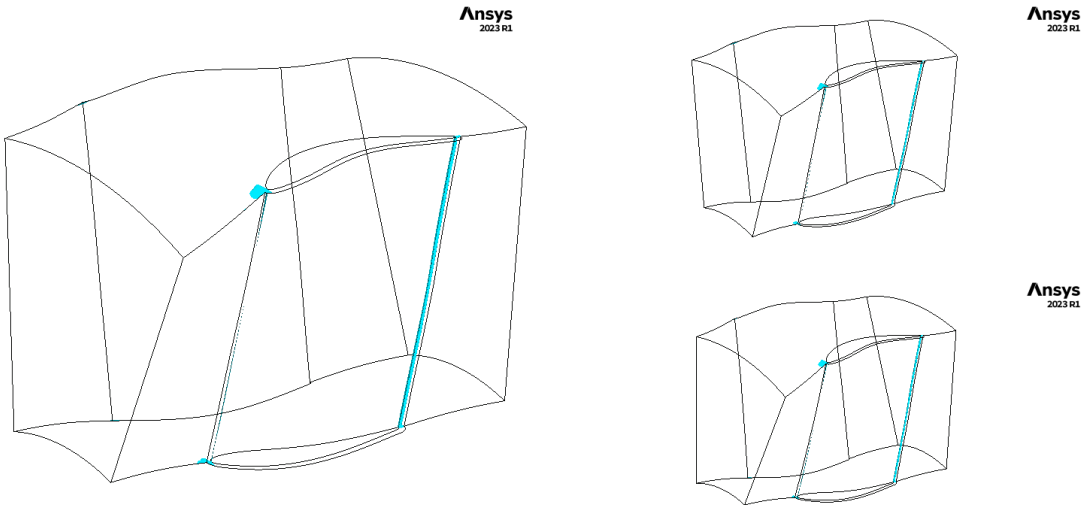

Figure 5.23: Isosurface of cyan color shows axial velocity of -0.1 m/s. To the left is design 1, top right is design 2 and bottom right is design 3. Contour shows negative velocity at design point.

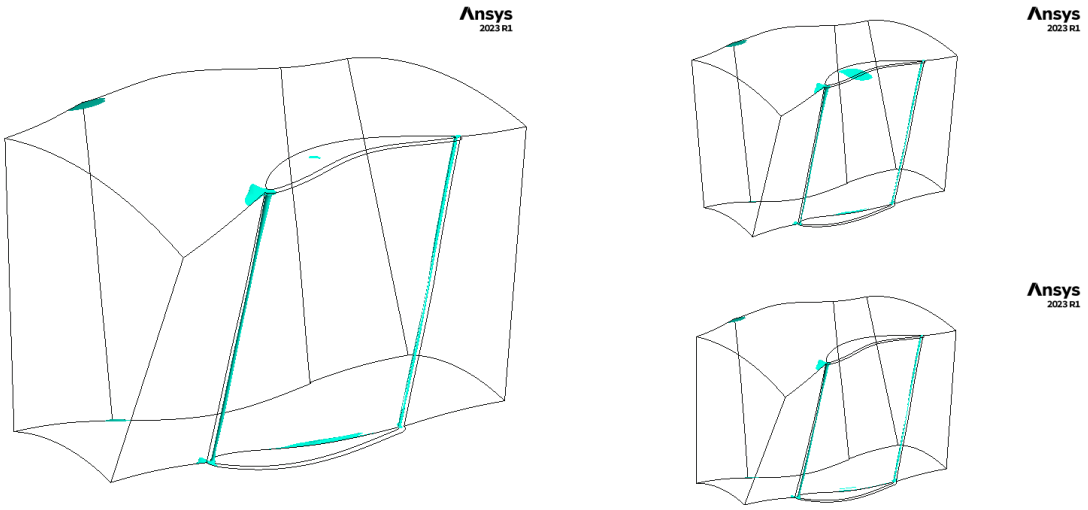

Figure 5.24: Isosurface of cyan color shows axial velocity of -0.1 m/s. To the left is design 1, top right is design 2 and bottom right is design 3. Contour shows negative velocity at off-design point of plus 10 degree inlet swirl.

Seen in figure 5.24, design 2 shows a slight increase in separation close to the shroud for the off-design point compared to designs 1 and 3. It can be seen in the figure that a slight increase of separation occurs along the hub vane side for the optimized design 1 compared to the two other designs, however since this increase is very small in comparison this is not considered a decisive result for choosing the best design. Off-design point for minus 10 degrees inlet swirl are shown for the designs in appendix B, where the designs show similar and low tendency for separation.

Looking at the wall shear stress for the designs at design point, it can be seen that the lowest stress occurs close to the shroud towards the trailing edge of the vane. Figures 5.25 and 5.26 show the wall shear stress at the pressure side of the vanes, whereas the tendency for separation can be seen in the second figure.

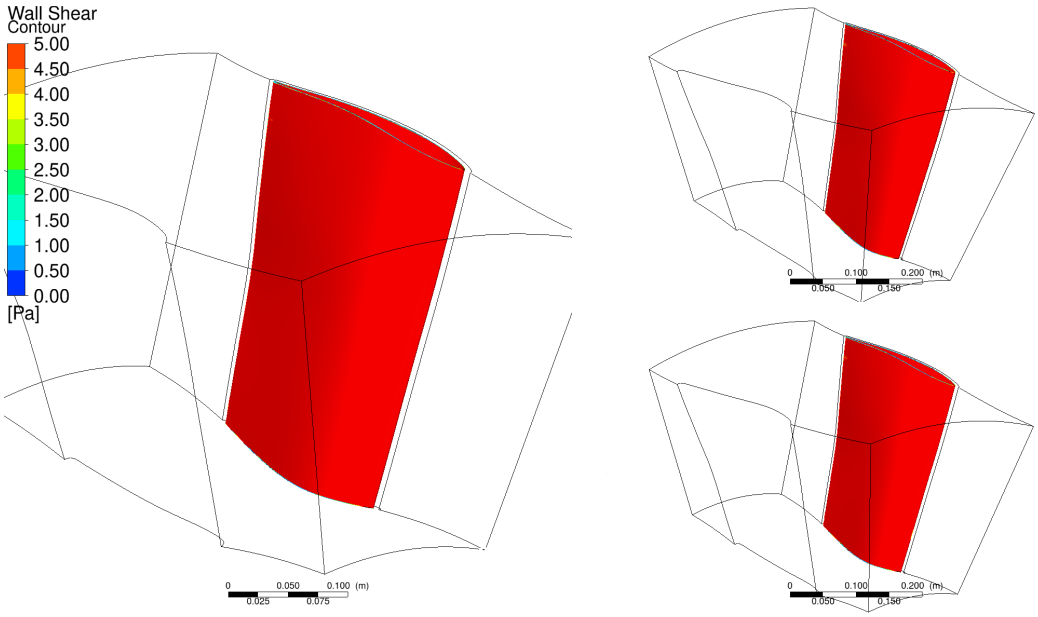

Figure 5.25: Wall shear stress contour plots at the vane surface for the three Pareto designs at design point. To the left is design 1, top right is design 2 and bottom right is design 3.

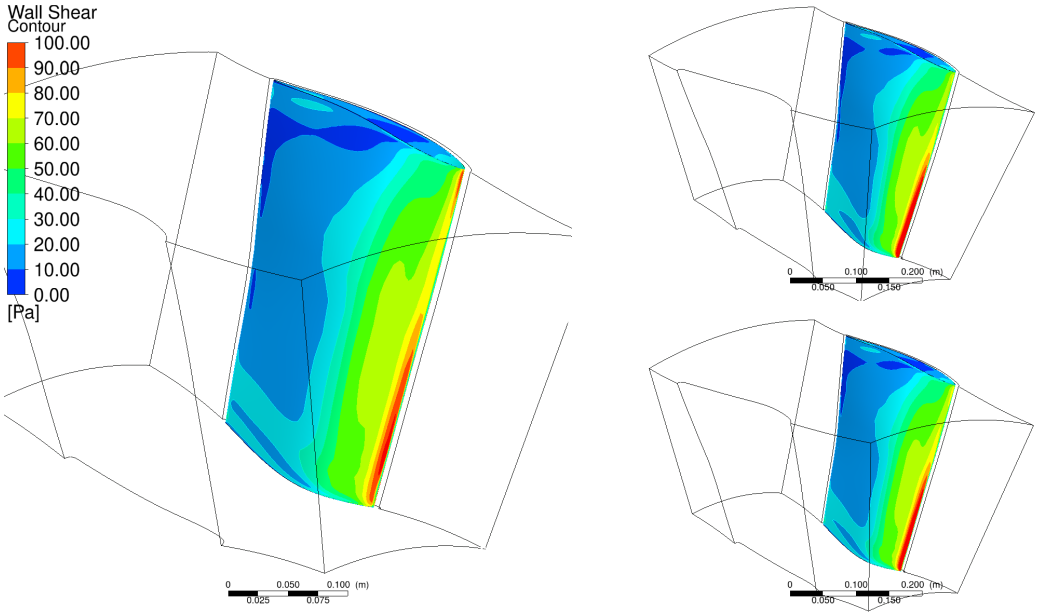

Figure 5.26: Wall shear stress contour plots at the vane surface for the three Pareto designs at design point. To the left is design 1, top right is design 2 and bottom right is design 3.

The wall shear stress for the designs at off-design of plus 10 degree inlet swirl is shown in figures 5.27 and 5.28 where all designs show low stress close to the trailing edge at around 80% span.

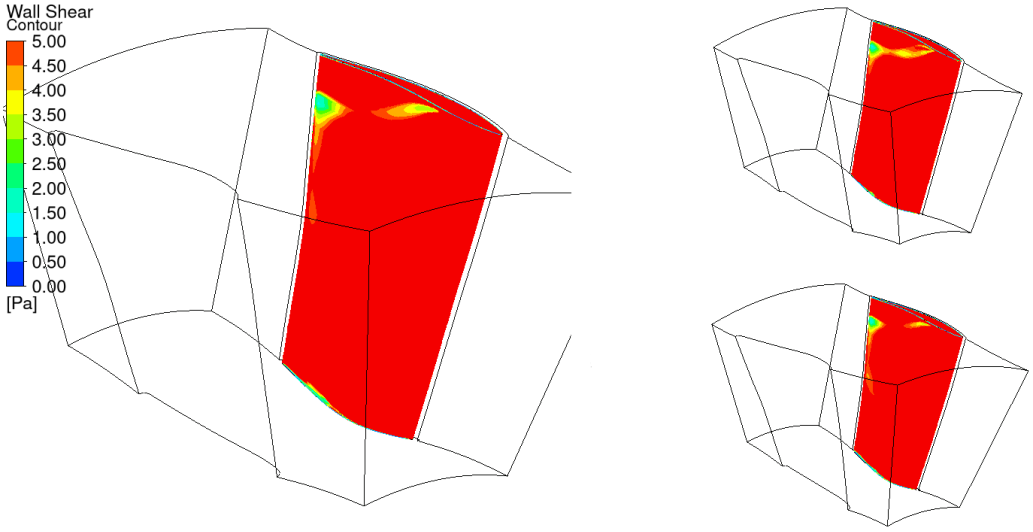

Figure 5.27: Wall shear stress contour plots at the vane surface for the three Pareto designs at off-design point plus 10 degree inlet swirl. To the left is design 1, top right is design 2 and bottom right is design 3.

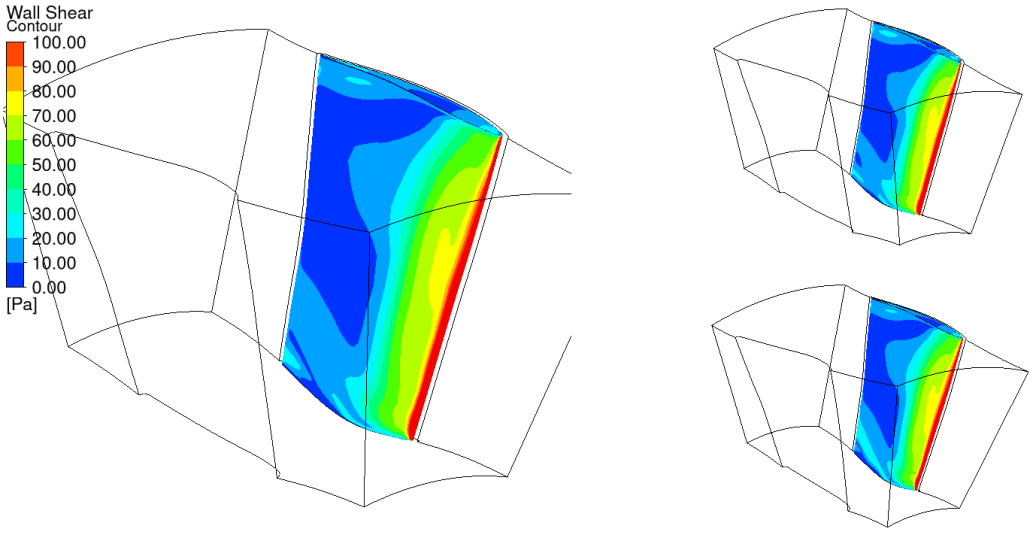

Figure 5.28: Wall shear stress contour plots at the vane surface for the three Pareto designs at off-design point plus 10 degree inlet swirl. To the left is design 1, top right is design 2 and bottom right is design 3

The designs for off-design of minus 10 is shown in appendix C in figures C.1 and C.2.

The total pressure loss for the three designs are analyzed and showed in figure 5.29.

The largest difference for the designs are shown at off-design point plus 10 degree inlet swirl angle.

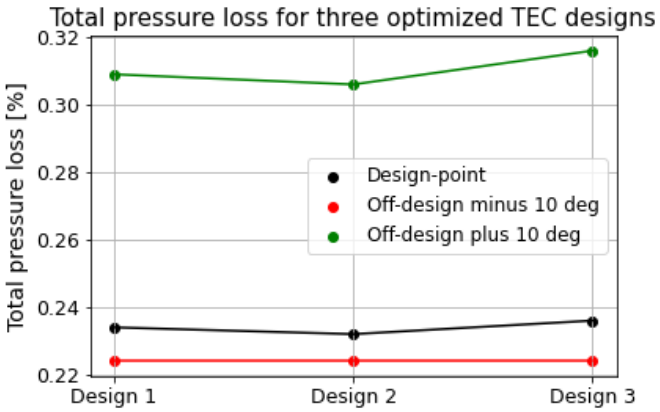

Figure 5.29: Total pressure loss for the three Pareto designs of the TEC

5.5 Final design

Given that the optimal design 1 show similar separation tendencies compared to the other two designs chosen from the Pareto front, it was decided to continue with design 1 for the acoustic study. The endwall contours of the optimized design and the baseline design are shown in figure 5.30. From the optimization an increase in endwall contour was found for minimizing the objective functions of lowering total pressure loss.

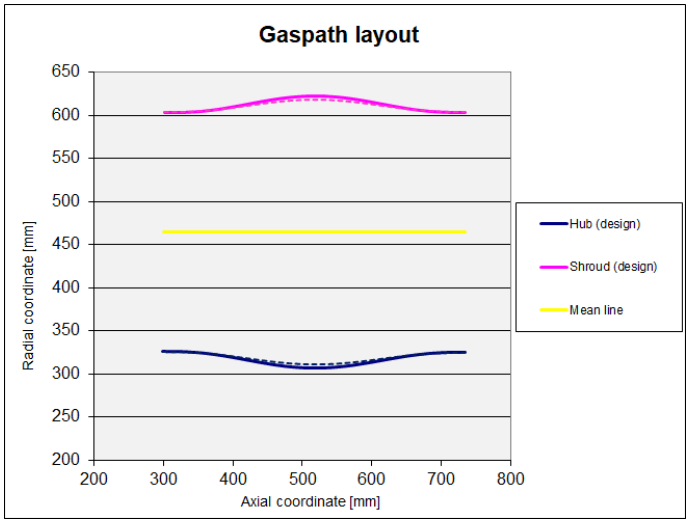

Figure 5.30: TEC endwall contours of the gaspath with the optimized design (thick line plot) and the baseline design (dashed plot)

The vane design is shown in comparison between the baseline and optimized design, seen in figure 5.31.

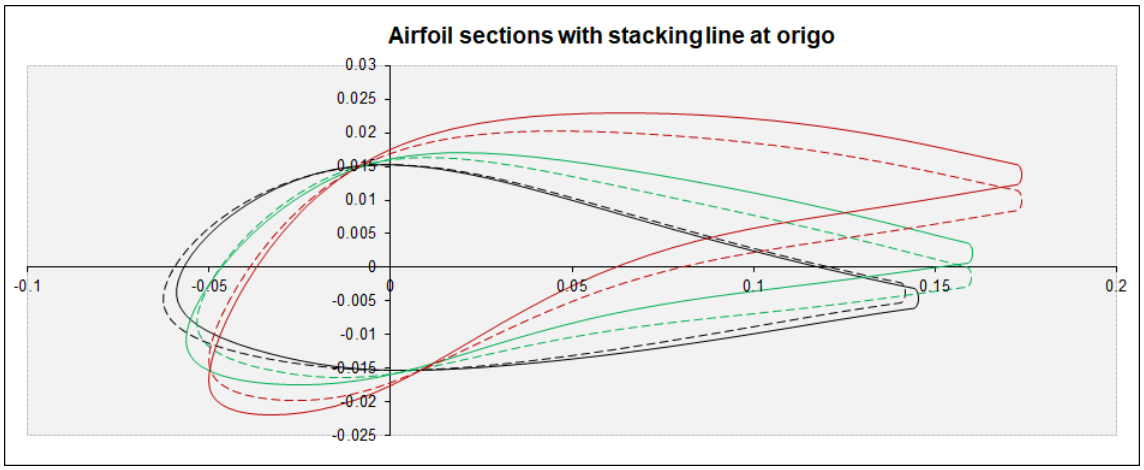

Figure 5.31: TEC airfoil section at 12.5% span (black plots), 50% span (green plots) and 87.5% span (red plots) for the baseline design. The dashed line plots show the airfoils for the baseline design and the solid lines show the optimized airfoil design.

Swirl profiles between the baseline design and the optimal design is shown in figure 5.32. By comparing the study from Vikhorev V. from section 1.3.1 with the TEC in this thesis, the outlet swirl angle profile varies mostly here within 2-3 degrees (from 12.5 to 87.5% span) when disregarding the hub and shroud angles. In Vikhorevs study the swirl angle varied within 4 degrees from hub to shroud for the same span interval, which shows good performance of the optimized TEC design.

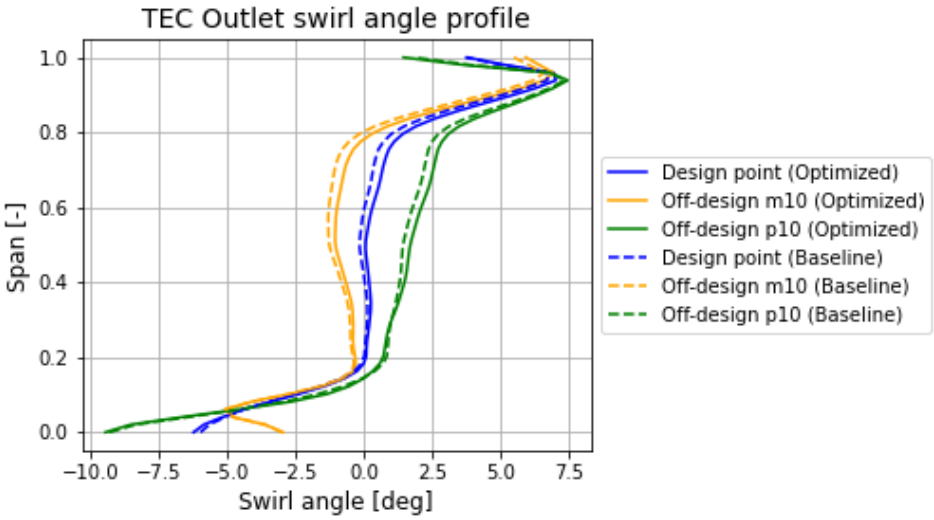

Figure 5.32: Swirl angle profiles for the baseline and optimized design of the TEC at design point and off-design points.

The total pressure loss between the two designs are shown in table 5.10. The small range in outlet swirl angle profile and total pressure loss between the baseline and optimized TEC design can be due to that the parameter range in the optimization

was too small, allowing the designs to vary only within a small range of response and parameter values, or that the baseline design was producing results very close to the wanted output response.

Table 5.10: Total pressure loss for the TEC baseline and optimized designs at design and off-design points.

	Baseline	**Optimized**	**Difference**
Design point	0.239%	0.234%	-2.30%
Off-design point m10	0.227%	0.224%	-1.54%
Off-design point p10	0.315%	0.309%	-1.84%

A comparison of the optimized design with the predicted response on the total pressure loss at design point and the difference in total pressure loss between flow conditions is seen in table 5.11.

Table 5.11: Comparison between the predicted total pressure loss from the MOP response surface for the optimized TEC design with the results from CFD.

	Response surface	**Optimized**	**Difference**
Total pressure loss at DP	0.235%	0.234%	-0.43%
Total pressure loss difference ϵ	0.0672	0.0008	-98.88%

6

Acoustic analysis results

The TEC design arrived at by optimization in the previous section has a stacking with zero lean angle. This optimal design is now compared acoustically to a design with 20 degrees positive lean. Noise emissions from the TEC was analyzed for hydrodynamic and acoustic waves traveling downstream from the LPT through the gaspath of the TEC. From analysis of the entropy contours of the TEC, the movement of hydrodynamic waves are captured, and from the pressure contours the movement of acoustic waves are captured. The noise levels were evaluated at outlet of the TEC and compared between the straight vane design and the leaned vane design. Results are shown for the waves of entropy and pressure contours.

The vane design of leaned guide vanes are evaluated for how the total pressure loss is affected by applying 20 degree lean, seen in table 6.1. A slight increase in total pressure loss can be seen for all flow conditions, where the largest increase is seen for the design point of about one percent.

Table 6.1: Total pressure loss presented for the optimized straight vane TEC design with the leaned TEC design.

	Straight	**Lean**	**Difference**
Total pressure loss at DP	0.234%	0.236%	+1.03%
Total pressure loss at m10	0.224%	0.226%	+0.85%
Total pressure loss at p10	0.309%	0.311%	+0.52%

For the contours of entropy for the straight vane design and leaned vane design, seen in figures 6.1 and 6.2 respectively, the wave patterns are seemingly similar. The hydrodynamic waves move with the mean flow, whereas the wave pattern follows the axial direction.

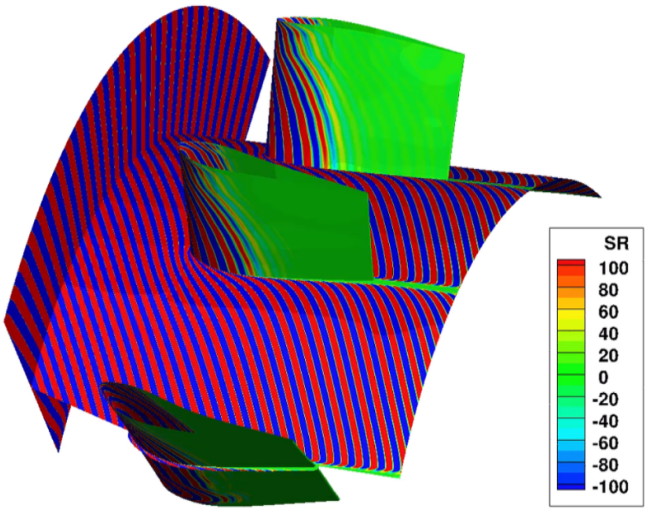

Figure 6.1: Entropy contour plot of the TEC where the waves from the inlet traveling downstream is seen as the cross flow of blue and pink waves. The figure is shown for the TEC with straight vanes.

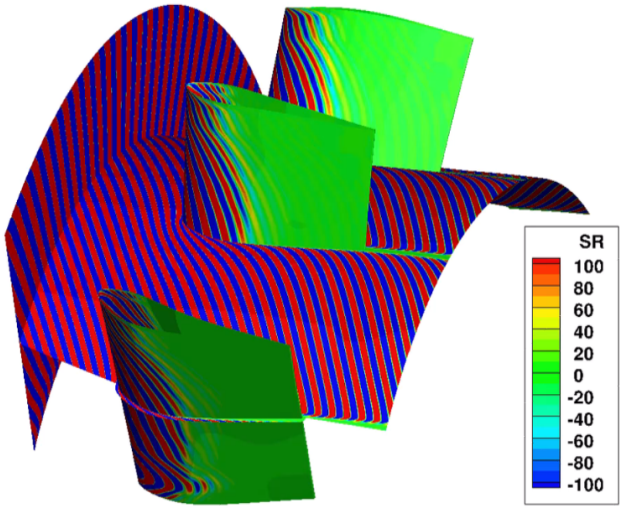

Figure 6.2: Entropy contour plot of the TEC where the waves from the inlet traveling downstream is seen as the cross flow of blue and pink waves. The figure is shown for the TEC with leaned vanes of 20 degrees.

Acoustic waves are shown in the pressure contours in figures 6.3 and 6.4. While it is difficult to visualize the movement of the waves, superposition and canceling of waves are seen in the blue and red pattern. The acoustic waves propagate at the speed of sound relative to the convection speed of the fluid. Acoustic waves can therefore at subsonic flow speeds propagate both up- and down-stream (all directions).

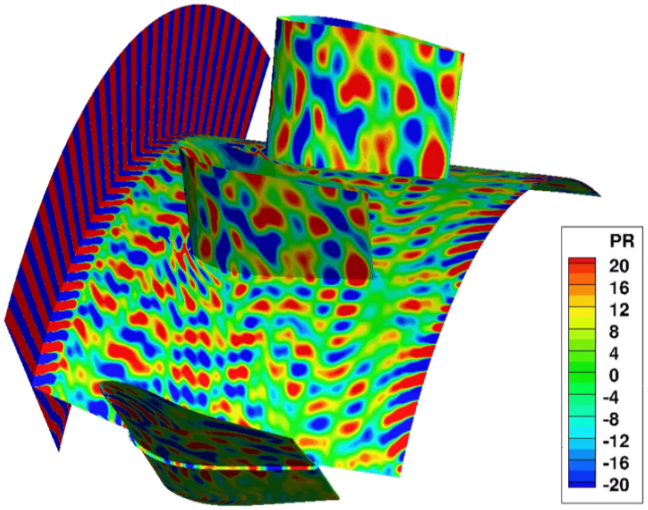

Figure 6.3: Pressure contour plot of the TEC where the waves from the inlet traveling through the TEC is seen as the blue and pink wave patterns. The figure shows the TEC with straight vanes.

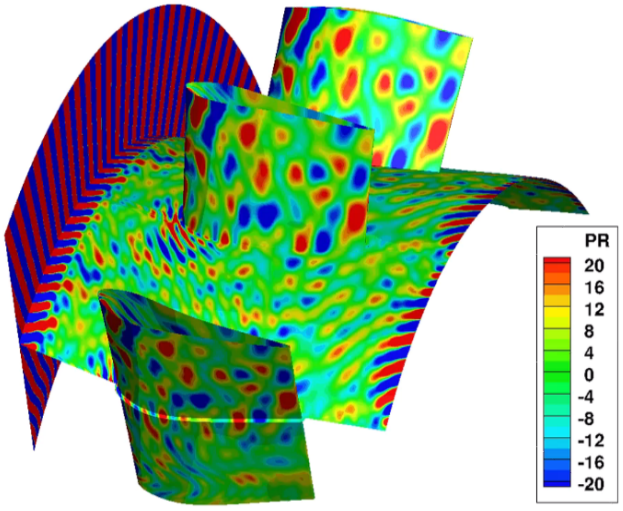

Figure 6.4: Pressure contour plot of the TEC where the waves from the inlet traveling through the TEC is seen as the blue and pink wave patterns. The figure shows the TEC with leaned vanes.

Results for the noise emissions from the TEC are evaluated for the power levels (PWL) of the straight and leaned vane design. The PWL is calculated by integrating the acoustic power levels over the TEC outlet, which is then analyzed and shown in table 6.2.

Table 6.2: Acoustic power levels [PWL dB] at 1BPF at outlet of the TEC.

Straight	**Lean**	**Difference**
104.3 [dB]	102.9 [dB]	-1.4

The seemingly small difference in PWL is put in perspective by the the logarithmic calculation between the power levels of the straight and leaned vanes. As the power P increase by double the amount, the PWL will increase at about 3 [dB] shown below.

- A $= 10 \cdot \log\left(\frac{P}{P_{ref}}\right)$
- B $= 10 \cdot \log\left(\frac{2 \cdot P}{P_{ref}}\right) \Rightarrow 10 \cdot \log\left(\frac{P}{P_{ref}}\right) + 10 \cdot \log(2) \simeq A + 3$

Therefore the decrease of 1.4 dB from having straight to leaned vanes show the significance of the noise level drop.

7
Conclusion

By analyzing the results for the ICD design response surface and Pareto design parameter values from the optimization it is evident in retrospect that the parameter ranges could have been larger. A reason for this could be that when keeping the criterion for the constraints as low as set in table 4.5, the optimization is limited in how much the geometry changes between optimized designs. Large design parameter ranges in the DOE increase the risk that some geometries generate large areas of separation, and therefore would be difficult to evaluate.

When estimating the boundary conditions for robust off-design conditions by only varying the inlet swirl angle with positive and negative 10 degrees, the total pressure at the inlet remains constant. Since the total pressure is defined at the inlet, the mass flow remains approximately the same, as the TEC turns the flow in the axial direction and the static pressure is the same at the outlet. Unless losses are very different for the investigated cases, the mass flow will be similar. Therefore when only varying the swirl angle, the absolute velocity changes, while keeping the same axial velocity. Using this method of robust off-design condition implies the consideration of the affect of keeping the other flow properties constant. In future studies, it would be beneficial to use more engine realistic off-design conditions where other flow properties, other than the swirl angle, also change when evaluating off-design conditions for robustness.

When creating a design space of the exact numbers of designs needed for the koshal designs from equation 3.7 the MOP generated response surfaces that gave unphysical results when the designs were run in the evolutionary algorithm. Due to this, the design space was increased by creating twice as many designs in order to increase the probability of finding an optimal design that produces physical results. With the increased data set of designs, the response surface still showed some deviation in response compared to the CFD evaluated designs from the optimization, seen in for the ICD design in table 4.9 and the TEC designs in table 5.11. A further iteration could have been made where designs that show a response close to the baseline design could have been added to the data set. The optimization would be run yet again, predicting the second order polynomial response surface for the designs which would be used in the evolutionary algorithm. This would ensure a more accurate behavior of response of the designs.

By comparing the off-design boundary conditions at EOR, which was used in the acoustic study, with the design point boundary conditions of inlet swirl angle from figure 5.1 it can be seen that the swirl between the two flow conditions vary at most 3 degrees. Analysis of the robust off-design boundary conditions, which was

used in the design and optimization process of the TEC, show that these boundary conditions are quite broad from the EOR off-design point in terms of swirl angle profile. When analyzing the wall shear stress for the off-design point of plus 10 degree inlet swirl profile in figure 5.27, it is evident that the separation tendency around 80-90% span would occur due to the large difference in swirl angles. The tendencies seen for the separation of the TEC has therefore not been concerning.

In summary the chosen designs for both the ICD and TEC show decreased total pressure loss relative to the baseline designs and both designs show good aerodynamic performance. This is considered of being able to turn the flow close to zero degree outlet swirl angle and keeping the boundary layers from separating. Lastly, the TEC noise level (PWL) was lowered for a leaned guide vane design by 1.4 dB.

Bibliography

[1] *ANSYS CFX 2023 R1: CFX-Solver Modeling Guide, Chapter 4: Turbulence and near-wall modeling, Subchapter 4.2 Modeling flow near the wall.* URL: https://www.ansys.com/.

[2] *ANSYS OptiSLang 2023 R1. Methods for Multi-Diciplinary Optimization and Robustness Analysis.* URL: https://www.ansys.com/.

[3] C. Florentina Balan. "CFD validation of a new gas turbine stage design with experimental data". In: *TRITA-ITM-EX 2022:24* (2022).

[4] J D Denton. "Loss mechanisms in Turbomachinery". In: *ASME: 93-GT-435* (1993).

[5] J. D. Denton and L. Xu. "The Trailing Edge Loss of Transonic Turbine Blades". In: *ASME 89-GT-278* (1989).

[6] *George Pechlivanoglou, CC BY-SA 3.0, via Wikimedia Commons.* URL: https://commons.wikimedia.org/wiki/File:Basic_theory_airfoil_basics.svg.

[7] Arthur J. Glassman. "Turbine design and application, NASA SP-290 Volume 1". In: (1972).

[8] Isak Jonsson et al. "Design and pre-test evaluation of a low-pressure compressor test facility for cryogenic hydrogen fuel integration". In: *Proceedings of ASME Turbo Expo 2021: GT2021-58946* (2021).

[9] P. Ligrani, G. Potts, and A. Fatemi. "Endwall aerodynamic losses from turbine components within gas turbine engines". In: *Propulsion and Power Research* (2017). ISSN: 2212-540X.

[10] Lejon M. et al. "Multidisciplinary design of a three stage high speed booster". In: *Proceedings of ASME Turbo Expo 2017: GT2017-64466* (2017).

[11] *Nasa aeronautics and space administration, Isentropic flow.* URL: https://www.grc.nasa.gov/www/k-12/airplane/isentrop.html.

[12] Wei Ning. *Significance of loss models in aerothermodynamic simulation for axial turbines.* 2000. ISBN: 9171705406.

[13] A. Olsson, G. Sandberg, and O. Dahlblom. "On Latin hypercube sampling for structural reliability analysis". In: *Structural safety* (2022). ISSN: 0167-4730. URL: https://www.sciencedirect.com/science/article/pii/S0167473002000395.

[14] *OptiSLang 2023 R1: Reliability Analysis, Appendix A: DOE scheme. R1: Reliability Analysis, Appendix A: DOE scheme.* URL: https://www.ansys.com/.

[15] Brian Stapleton Stratford. "The prediction of separation of the turbulent boundary layer". In: *Journal of Fluid Mechanics* 5 (1959), pp. 1–16. URL: https://api.semanticscholar.org/CorpusID:122258979.

[16] *Stratford's separation criterion*. URL: https://www.cfd-online.com/Wiki/Stratford%5C%27s%5C_separation%5C_criterion.

[17] V. Vikhorev and V. Chernoray. "Experimental Flow Analysis in a Modern Turbine Rear Structure with 3D Polygonal Shroud Under Realistic Flow Conditions". In: *European Conference on Turbomachinery Fluid Dynamics and Thermodynamics* (2021). DOI: http://dx.doi.org/10.29008/etc2021-539.

[18] V. Vikhorev, V. Chernoray, and O. Thulin et al. "Detailed Experimental Study of the Flow in a Turbine Rear Structure at Engine-Realistic Flow Conditions". In: *Journal of Turbomachinery* 143(9) (2021). DOI: http://dx.doi.org/10.1115/1.4050451.

[19] V. Vikhorev, I. Jonsson, and M. Tokarev et al. "Experimental study on the low-pressure turbine wake interaction and development in the turbine rear structure". In: *9TH EUROPEAN CONFERENCE FOR AERONAUTICS AND SPACE SCIENCES* (2022). DOI: http://dx.doi.org/10.13009/EUCASS2022-6151.

[20] V. Vikhorev et al. "The influence of the vane lean on the flow in a turbine rear structure". In: *ICAS2022, 33rd congress* (2022).

[21] Fredrik Wallin. "Flow Control and Shape Optimization of Intermediate Turbine Ducts for Turbofan Engines". PhD thesis. Chalmers University of Technology, 2008.

[22] Z. Wang et al. "Research on the lean and swept optimization of a single stage axial compressor". In: *Engineering Applications of Computational Fluid Mechanics* (2021). DOI: 10.1080/19942060.2020.1862708.

A

Appendix

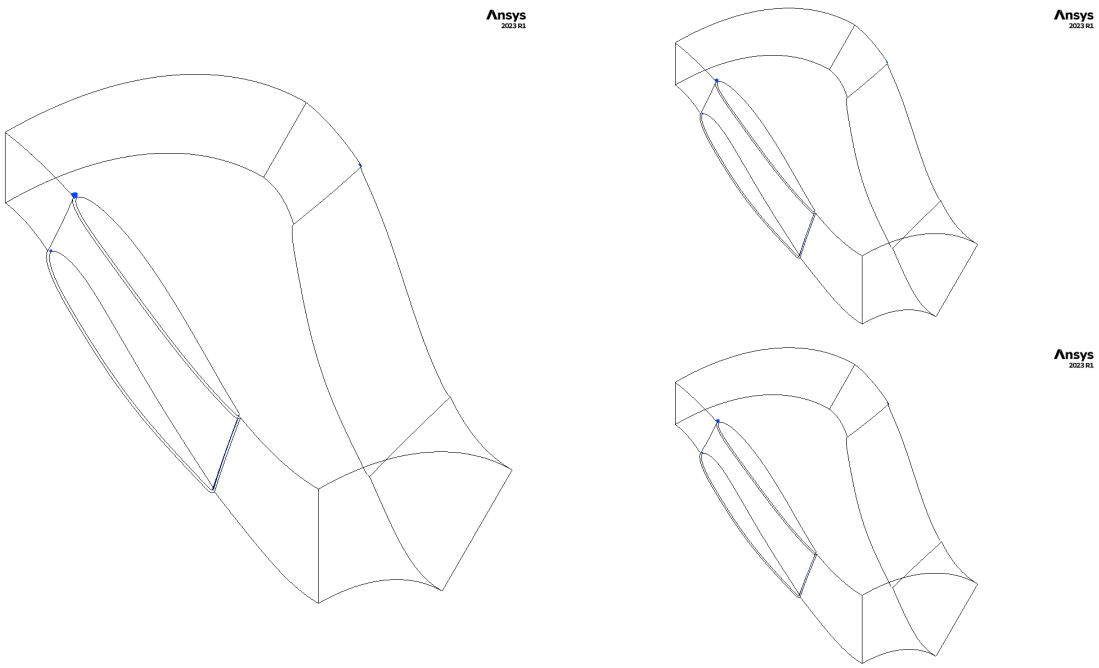

Figure A.1: Isosurface for velocity of -0.01 m/s showing for the three ICD designs at design point from the Pareto front in the EA optimization. Design 1 is in the left most figure, following design 2 and design 3 in the top and bottom right figures respectively.

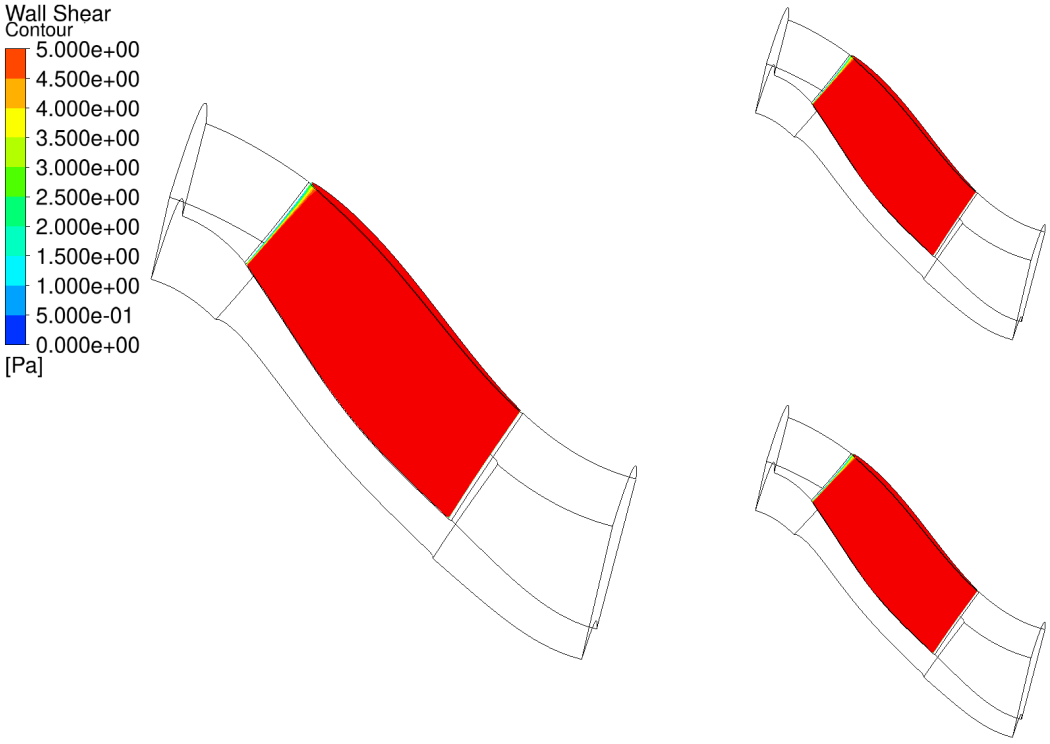

Figure A.2: Contour plots of the three ICD designs at design point from the Pareto front in the EA optimization. Design 1 is in the left most figure, following design 2 and design 3 in the top and bottom right figures respectively.

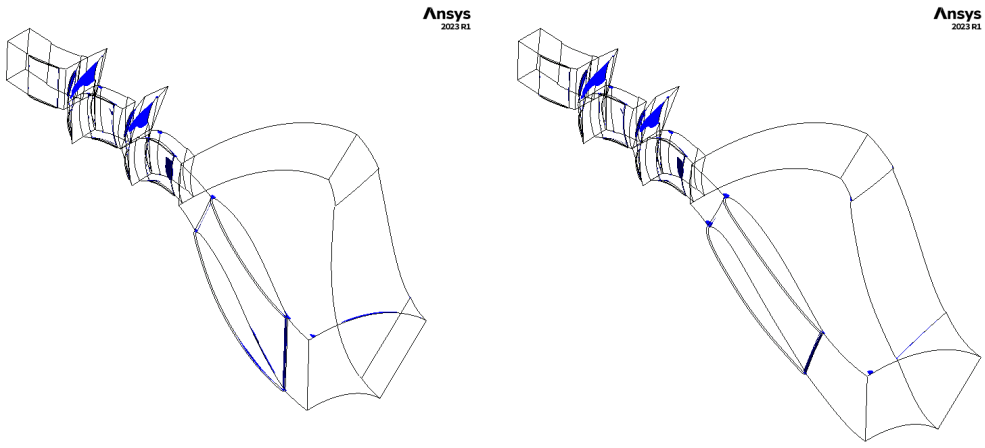

Figure A.3: Whole compressor system with the old and optimized design included in the left and right figures respectively. Isosurface of blue color shows negative axial velocity of -0.1 m/s at off-design point.

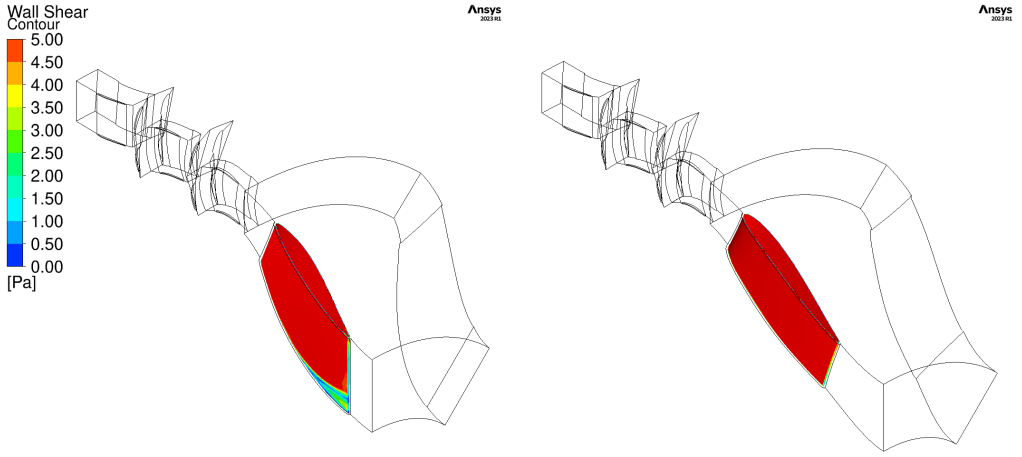

Figure A.4: Whole compressor system with the old and optimized design included in the left and right figures respectively. Contour of wall shear stress is shown at design point.

B

Appendix

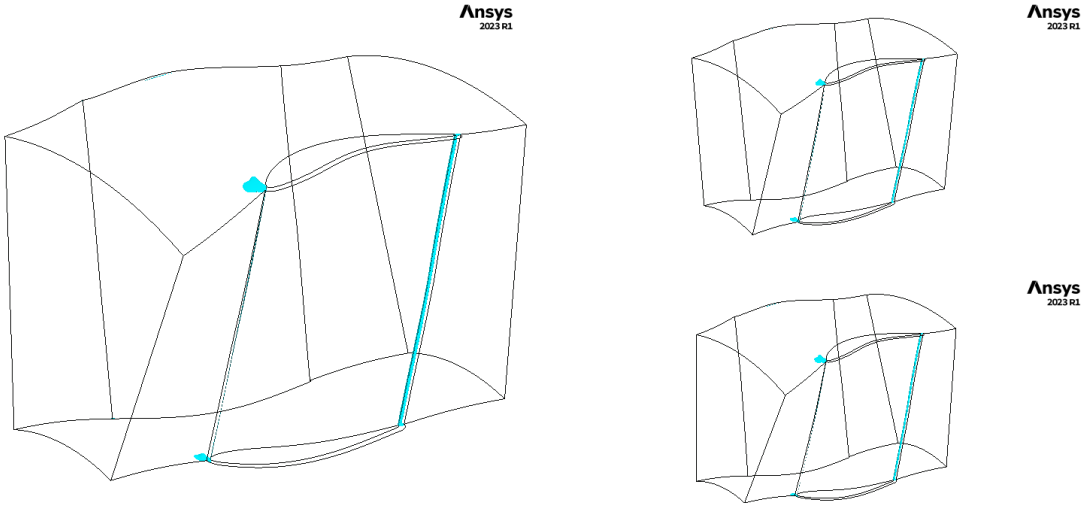

Figure B.1: Isosurface of cyan color shows axial velocity of -0.1 m/s. To the left is design 1, top right is design 2 and bottom right is design 3. Contour shows negative velocity at off-design point of minus 10 degree inlet swirl.

C

Appendix

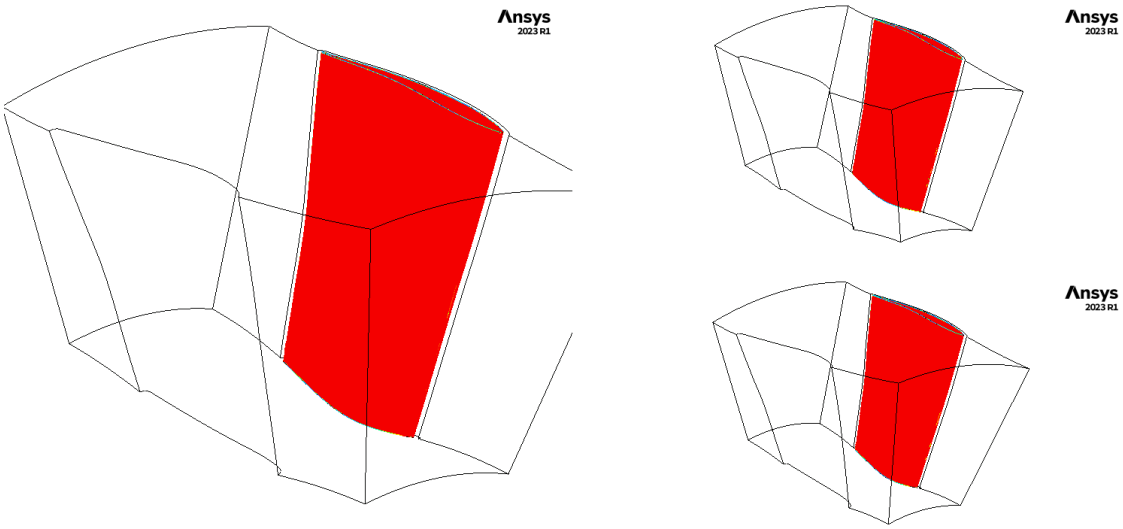

Figure C.1: Wall shear stress contour plots at the vane surface for the three Pareto designs at off-design point minus 10 degree inlet swirl. To the left is design 1, top right is design 2 and bottom right is design 3

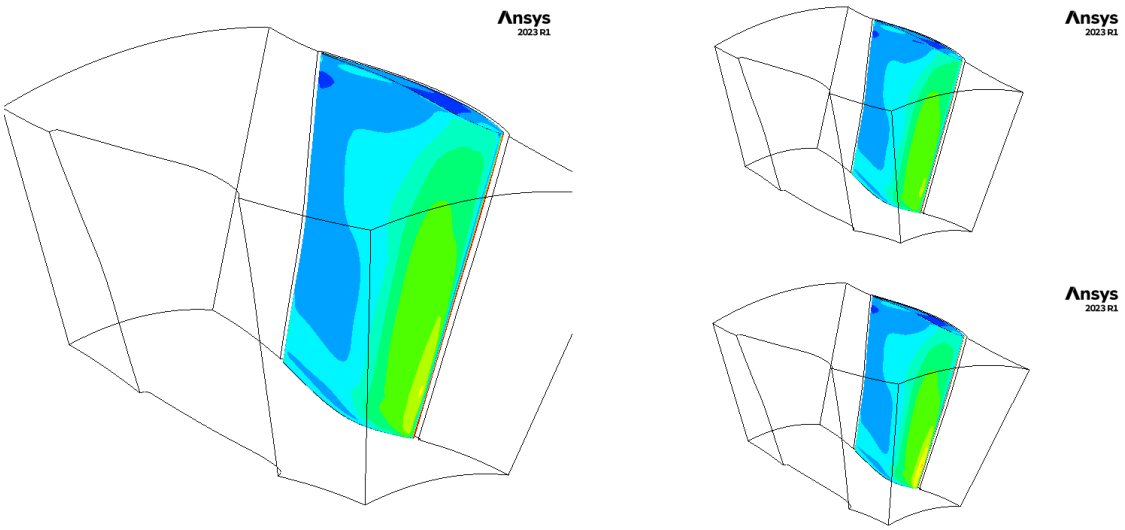

Figure C.2: Wall shear stress contour plots at the vane surface for the three Pareto designs at minus 10 degree inlet swirl. To the left is design 1, top right is design 2 and bottom right is design 3.

DEPARTMENT OF SOME SUBJECT OR TECHNOLOGY
CHALMERS UNIVERSITY OF TECHNOLOGY
Gothenburg, Sweden
www.chalmers.se

CHALMERS
UNIVERSITY OF TECHNOLOGY